The Pennsylvania State University

The Graduate School

Engineering Science and Mechanics Department

# SUPPRESSION OF CIRCULAR BRAGG PHENOMENON IN CHIRAL SCULPTURED THIN FILMS PRODUCED WITH SIMULTANEOUS ROCKING AND ROTATION OF SUBSTRATE DURING SERIAL BIDEPOSITION

A Thesis in

Engineering Science

by

Stephen E. Swiontek



Submitted in Partial Fulfillment
of the Requirements
for the Degree of

Master of Science

May 2012

The thesis of Stephen E. Swiontek was reviewed and approved* by the following:

Akhlesh Lakhtakia
The Charles G. Binder (Endowed) Professor of Engineering Science and Mechanics
Thesis Co-Adviser

Jian Xu
Associate Professor of Engineering Science and Mechanics and Adjunct Professor of Electrical Engineering
Thesis Co-Adviser

Judith A. Todd
P. B. Breneman Department Head Chair
Head of the Department of Engineering Science and Mechanics

*Signatures are on file in the Graduate School

# ABSTRACT

A sculptured thin film (STF) is produced by physical vapor deposition, whereby a collimated vapor flux is directed obliquely onto a moving substrate on which the STF is deposited. The STF comprises parallel and identical nanocolumns of a certain shape sculptured by substrate motion. Substrate rotation produces chiral STFs whose nanocolumns are helical. Chiral STFs produced by serial bideposition, which either actually or effectively involves two vapor fluxes, possess large local linear birefringence and evince highly intense optical activity, both of which properties are attractive for optical sensor, filter, and display technologies. Specifically, chiral STFs exhibit the circular Bragg phenomenon for normally incident light: in a certain spectral regime, either left- or right-circularly polarized light is preferentially reflected.

Theoretical modeling has shown that if the substrate is rocked, in addition to rotation, the circular Bragg phenomenon is suppressed, even though the deposited thin film should still have a chiral morphology. Instead, an ordinary Bragg phenomenon is exhibited which is insensitive to the polarization state of the incident light. Therefore, an ordinary Bragg filter can be made with just one material, instead of as a quarter-wave stack that requires the deposition of two materials.

For this work, ZnSe chiral STFs were fabricated with/without substrate rocking, and their transmittance spectrums for linear- and circular-polarized incident light were measured. During fabrication, a collimated vapor flux was directed at a vapor flux angle

of either 20° or 25° with respect to the substrate plane, which was rotated at 0.5 rpm in a low-pressure vacuum chamber at a base pressure of $1.5 \times 10^{-5}$ Torr. At the same time, the substrate was rocked with an amplitude of 5°, 10°, 15°, or 20° depending on the initial starting value of vapor flux angle. The rocking period and the rotation period were identical. All chiral STFs produced were 9-periods thick, with the spatial period being 330 nm. With sufficient rocking amplitude, the discrimination between left- and right-circularly polarized (RCP and LCP) light nearly vanished, whereas similar Bragg phenomenons for s- and p-polarized light were observed. Thus, chiral STF technology can be used to produce both ordinary and CP Bragg filters.

# TABLE OF CONTENTS

## LIST OF FIGURES

# LIST OF TABLES

# ACKNOWLEDGEMENTS

I will take this space to thank my adviser and co-adviser, Dr. Akhlesh Lakhtakia and Dr. Jian Xu, respectively, for their continued support and helpful conversations throughout this research endeavor. I thank Dr. Carlo Pantano for permission to prepare and deposit thin films in his laboratory co-operated by Dr. Lakhtakia. I also thank Dr. Sean Pursel and Drew P. Pulsifer for their advice on deposition methods of chiral sculptured thin films. Gratitude is extended to Drew P. Pulsifer for capturing SEM images of all thin films presented in this thesis. I am also grateful towards the Charles Godfrey Binder Endowment which partially funded this work. Finally, I profusely thank my family, friends, and colleagues for their unquestionable love and support which sustained me throughout this work.

**This thesis is hereby dedicated to the reader.*

# CHAPTER 1

# INTRODUCTION

Structurally chiral materials, such as cholesteric liquid crystals [1] and chiral sculptured thin films, discriminate between left- and right-circularly polarized plane waves [2]. Provided a structurally chiral material is sufficiently thick and the wavelength of a normally incident planewave lies in a spectral regime called the circular Bragg regime, high reflectance is observed if the handedness of the incident plane wave is the same as the structural handedness of the structurally chiral material, but not otherwise [3]. This phenomenon is called the circular Bragg phenomenon [4] and is exploited for designing circular-polarization filters [5]. A similar discrimination between left- and right- circularly polarized plane waves is found for obliquely incident plane waves too, but that discrimination disappears for highly oblique incidence. Oblique incidence was not considered for this thesis.

The objective of the research undertaken for this thesis was to fabricate and optically characterize a structurally chiral thin film that does *not* discriminate between left- and right- circularly polarized plane waves but still exhibits the Bragg phenomenon. This work follows a theoretical prediction [6] that if a sculptured thin film is grown by physical vapor deposition while the substrate is being simultaneously rotated *and rocked*, then the STF will have a chiral morphology and will exhibit the Bragg phenomenon, but will not be sensitive to the polarization state of the normally incident plane wave.

This chapter provides a general overview of the fabrication, growth mechanics, and optical characteristics of sculptured thin films. Furthermore, circular-polarization-

independent mirrors, particularly made of STFs are discussed. An outline of this thesis concludes the chapter.

## 1.1 Thin films

Thin films are fabricated by transporting individual atoms and/or molecules onto a substrate by physical or chemical methods [7]. The basic properties of thin films, such as their electrical, mechanical, chemical, structural, and optical characteristics, are different on the micrometer and nanometer length scales than those of bulk materials—due to morphological effects arising from deposition techniques [8]. Specific thin-film deposition techniques are devised for specific applications to exploit their morphologically dependent properties. Among other industries, semiconductor electronics, mechanical, and optical-coating industries employ a multitude of thin films.

The specific fabrication technique has a large impact on the properties of a thin film. Physical vapor deposition (PVD) techniques transfer kinetic energy [9] to the atoms of a source material to overcome their binding energy. These energized atoms are ejected into a low-pressure environment and are then allowed to condense onto the surface of a substrate. Many ways exist to transfer kinetic energy—sputtering [10], electron-beam deposition [11], thermal evaporation [12], and laser-pulse ablation [13], among others. These PVD techniques have been widely used in industry for over a century.

In chemical vapor deposition (CVD), gases are introduced into the deposition chamber that will react and form the desired thin film on the surface of a substrate [14]. Either a single gas is used that will decompose when heated to supply the necessary component or components for the thin film, or several gases are used which will react and

form the thin film. The reaction should take place on the surface of the substrate but can sometimes occur above it. Above-surface reactions can create particles that form above the substrate, but these particles can drop onto the surface of the filim causing it to have pinholes or a low density [15].

Molecular-beam epitaxy (MBE) is a process for growing layers of atom-thick films. MBE can be used to deposit a wide variety of materials, ranging from semiconductors to metals to oxides; however, it is most commonly used for semiconductor deposition. In this process, beams of atoms or molecules in an ultra-high vacuum environment are incident onto a heated substrate. The arriving atoms form a crystalline layer on the surface of the substrates; thus, the thin film is epitaxial [16]. A wide range of structures have been made with MBE for quantum-well devices [17] and superlattices [18], all with precise control of film composition during growth. However, there are two main drawbacks to MBE. First, MBE systems are extremely expensive (~ $1M per system). Second, MBE is very time-consuming in research and even in industrial settings.

Atomic-layer deposition (ALD) is a vapor-phase, self-limiting, thin-film deposition technique where a substrate is exposed to two different and alternating precursors, laying down single-layers of the desired thin-film material onto the surface of the substrate during each cycle. [19]. ALD allows for conformal deposition of atomic layers and can reproduce features on the surface of the substrate very accurately [20]. Furthermore, ALD can produce very thin and dense films. However, similar to MBE, it is a slow and expensive technique.

Decher and co-workers developed the Layer-by-Layer (LbL) technique for the deposition of ultra-thin films [21]. This simple and versatile technique has been adopted for fabricating thin films with tailored properties from aqueous solutions (and suspensions) of molecules, polymers, or nanoparticles. A charged substrate spontaneously and sequentially adsorbs oppositely charged materials from dilute aqueous solutions. During the deposition process, the charged substrate is dipped in a solution of either a cationic or anionic polyelectrolyte for a desired period of time. Adsorption of the molecules on the exposed surface of the substrate takes place when the concentration of the charged species is sufficient enough to completely reverse the charge at that surface. The process is then repeated with a solution of either an anionic or cationic polyelectrolyte [22].

Spin coating is a physical technique used to form uniform thin films on flat substrates. Essentially, an excess amount of a solution is placed onto the substrate, which is then rotated at high angular speeds in order spread the liquid evenly over the substrate. Once the desired film thickness has been achieved, the rotation is stopped while any excess fluid is spun off the substrate [23].

I used resistive-heating PVD for all work in this thesis. In this technique, a source material is heated to release an atomic vapor flux which propagates towards a substrate on which the film is grown [24]. The source material is placed in a boat or crucible of a high-melting-temperature material through which an electric current is passed in order to achieve energy transfer from the boat/crucible to the source material [9]. This is a widely used technique in industry and research laboratories.

## 1.2 Sculptured thin films

Sculptured thin films (STFs) are a class of nano-engineered, porous, unidirectionally nonhomogeneous, and anisotropic thin films that can be fabricated using PVD techniques such as thermal evaporation [25], electron-beam PVD (EBPVD) [26], sputtering [27], and pulsed-laser deposition [28]. They have also been fabricated through chemical techniques such as CVD [29].

In any of these methods, a collimated vapor flux of the material to be deposited is made. This flux is directed obliquely onto a substrate which can be rocked and/or rotated about certain axes. Adatomic self-shadowing without substrate rotation gives rise to columnar morphology of the film growing on the substrate. This film, comprising parallel and tilted nanocolumns, is called a columnar thin film (CTF). When substrate rotation and/or rocking also occurs during deposition, the nanocolumns acquire a common shape and the film is called a sculptured thin film (STF) [30]. Growth methods, morphologies, and optical properties of STFs are discussed further in this chapter.

### 1.2.1 CTF deposition methods, growth mechanics, and morphology

Columnar thin films are grown as the direct result of self-shadowing at the length-scale of arriving adatoms (clusters of atoms of the source material arriving on the surface of the substrate) [31].

They are typically fabricated in low-pressure environments with low-adatom-mobility conditions. Self-shadowing can be explained as follows. When the evaporant material nucleates on the surface of the substrate, the region immediately behind it does

not receive any further adatoms because this location falls in the "shadow" of the growing nucleus. Therefore, the arriving adatoms will only be deposited onto the nucleated sites, resulting in the formation of nanocolumns.

It is accepted that the first CTF was made by Kundt in 1886 [32] by using oblique-angle deposition (OAD). Figure 1.1 shows the schematic of a low-pressure thermal evaporation system with a boat which contains the source material. A current is passed through the boat, which heats the source material to launch a collimated vapor flux. The incoming vapor flux, comprising adatoms with low mobility, adheres to the surface of the substrate through self-shadowing and forms parallel and tilted nanocolumns.

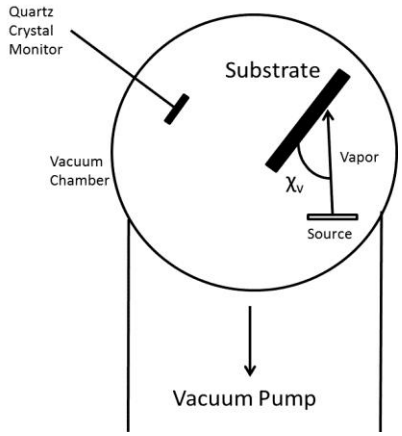


**Figure 1.1:** Schematic of a traditional PVD system for fabricating columnar thin films (adapted from [30]). The vapor flux is incident on the substrate at angle $\chi_v \in (0°, 90°]$ with respect to the substrate plane.

Figures 1.2 (A) and (B) show how different oblique angles of incidence $\chi_v$ dictate CTF morphology. Figure 1.2(C) displays a schematic which relates $\chi_v$ to the tilt angle $\chi$ of the growing nanocolumns with respect to the substrate plane. CTFs with lower values of $\chi_v$ (~ 5°) result in less dense and more porous films, whereas higher values of $\chi_v$ (~ 22.5°) result in highly dense and less porous films [33]. CTFs can have pores on the order of 30-300 nm [33]. Arriving adatoms form 1-to-3 nm clusters which initially form on the substrate, as long as the substrate temperature $T$ is below a third of the source material's melting temperature $T_m$ (i.e., $T/T_m$ <0.3). These nucleation clusters yield cone-shaped nanocolumns which acquire the shape of a matchstick within 20-30 nm of growth [30]. Accordingly, in the visible and infrared regimes, a CTF performs optically like a biaxial crystal [48], just like Kundt had guessed without the benefit of scanning electron microscopy (SEM).

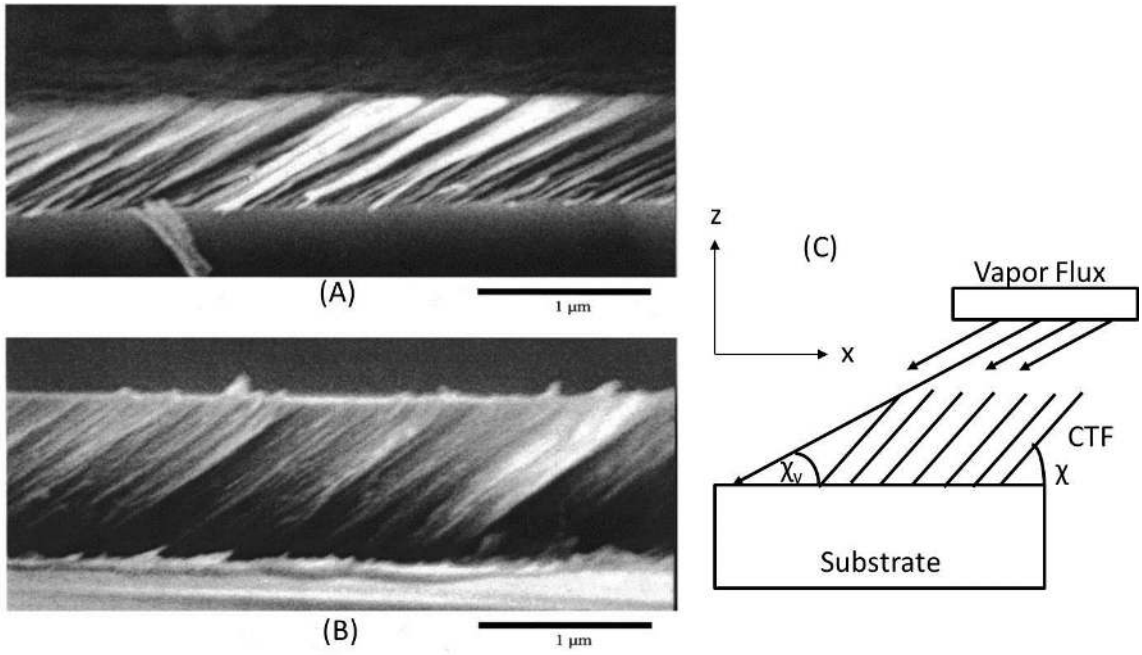


**Figure 1.2:** SEM images of a thermally evaporated CTF of $MgF_2$: (A) $\chi_v = 3°$ and (B) $\chi_v = 22.5°$ [33]. (C) The vapor flux angle $\chi_v$ is usually smaller than the tilt angle $\chi$ of the nanocolumns of the CTF; $\chi \geq \chi_v$. The morphologically significant plane of the CTFs depicted in these figures is the *xz* plane.

Structure zone models (SZMs) [34] were developed in order to classify both the cross-sectional and top-surface morphologies of evaporated metallic and oxide films. Figure 1.3 shows the SZM that has been developed over several decades that explain morphology zones for CTFs and STFs.

In Zone 1, tapered grains define the morphology. Zone 2 exhibits columnar crystalline grains resulting from higher ($T/T_m$) values which permit the diffusion of surface adatoms. Zone 3 shows increased grain size and lacks columnar morphology, making it unuseful for STF technology. Messier *et al.* [35] further explained the evolution

of morphology as a function of film thickness, thereby connecting the atomic-level understanding of self-shadowing and the SZM. They presented a cluster-based model to explain the regime between Zone 1 and Zone 2 [35]. In between Zones 1 and 2 lie Zones T and M. In Zone T, consisting of densely packed fiberous grains, the morphology does not offer long-range structures beyond the nanometer length-scale and is directly related to argon pressures. In Zone M, dome-shaped matchstick morphology is present. This is the most attractive zone for growing STFs.

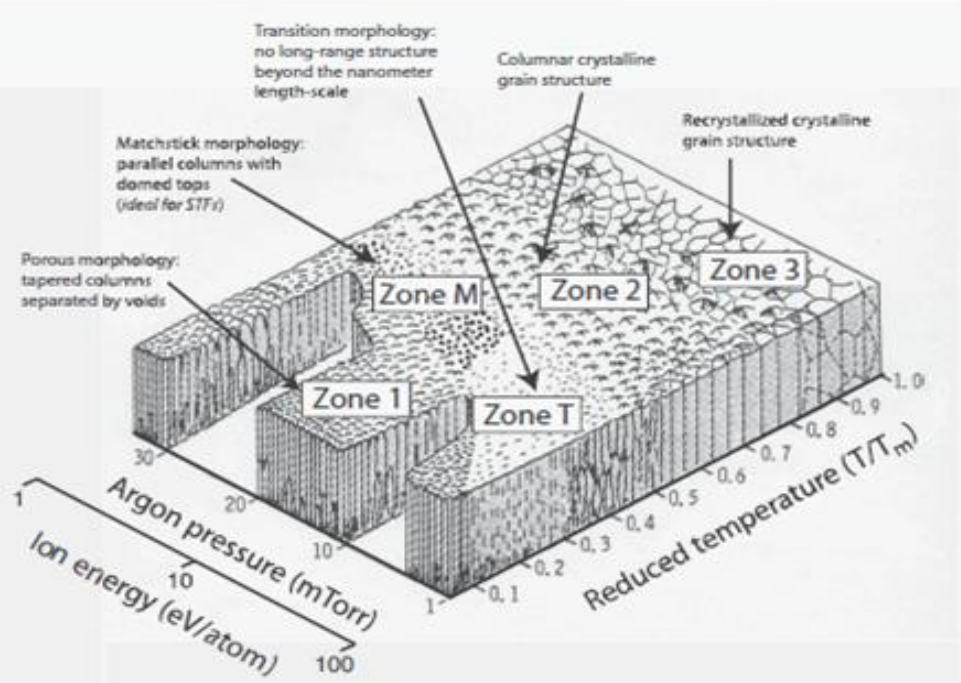


**Figure 1.3:** The currently accepted version of the SZM for CTFs [36]. Argon pressure in mTorr and the ratio $T/T_m$ of the substrate temperature $T$ and the melting point $T_m$ of the source material are the independent variables of deposition that govern morphology [35].

### 1.2.2 STF deposition methods, growth mechanics, and morphology

STFs are modifications of CTFs in which the nanocolumnar growth direction can be changed at will during growth. The term STF was first coined in 1997 by Lakhtakia and Messier [30], even though a few earlier examples did exist.

Most importantly, in 1959, Young and Kowal illustrated that periodic STFs with chiral (i.e. handed) morphology exhibits a signature of the circular Bragg phenomenon [36]. These scientists deliberately rotated the substrate about the $z$ axis (which passes normally through the center of the substrate) at a uniform rate during deposition, in order to fabricate calcium-fluoride films comprising chiral and parallel nanocolumns perpendicular to the substrate plane. These films are appropriately called chiral STFs because they possess structural handedness. Young and Kowal believed that "the activity of a helically deposited film could be due to the co-operative action of a helically symmetrical arrangement of crystallites, growth, or voids" [36]. However, the dielectric polarization properties can only be explained by a rotating anisotropic permittivity dyadic emerging from the helical morphology [37], but that was not confirmed until 1995 when Robbie *et al*. [38] examined SEM images of newly grown chiral STFs. Figure 1.4 shows an example of a chiral STF made by evaporating silicon dioxide [39].

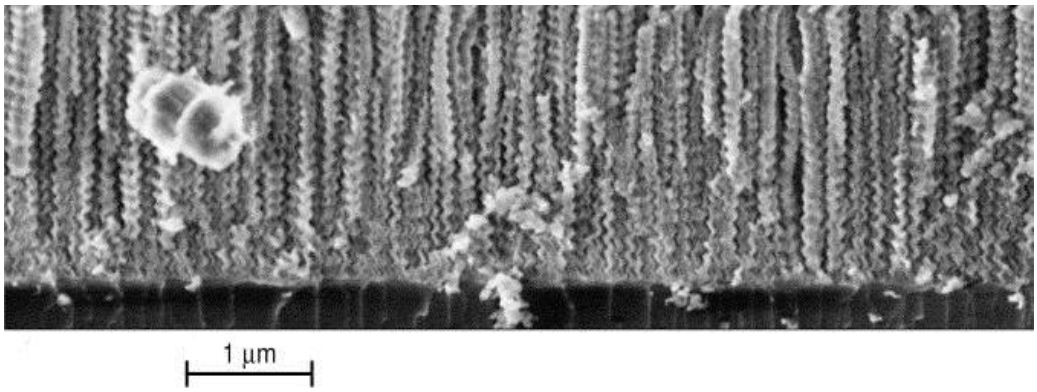


**Figure 1.4:** SEM image of an STF made by evaporating silicon dioxide displaying a chiral morphology [39].

By this time it was evident that a wide variety of nanocolumnar morphologies were possible through the control of two axes of substrate rotation. Along with the potential to evaporate a wide variety of materials, a wide variety of nanocolumnar morphologies should lead to numerous applications [40]. The modulation of these two fundamental axes leads to two canonical classes of STFs termed:

(i) sculptured nematic thin films (SNTFs) [31] and

(ii) thin-film helicoidal bianisotropic mediums (TFHBMs) [30, 38].

SNTFs are fabricated by rocking about an axis that is tangential to the substrate plane. By controlling the rocking of the substrate about this axis, several different morphologies can be realized. These can include zig-zags, C-, and S- shapes [41]. TFHBMs are fabricated when the incoming vapor flux is obliquely directed onto a substrate normal to the vapor flux and the substrate is rotated, thereby yielding chiral

morphology. Periodic TFHBMs are called chiral STFs. Figure 1.5 shows examples of several STF morphologies.

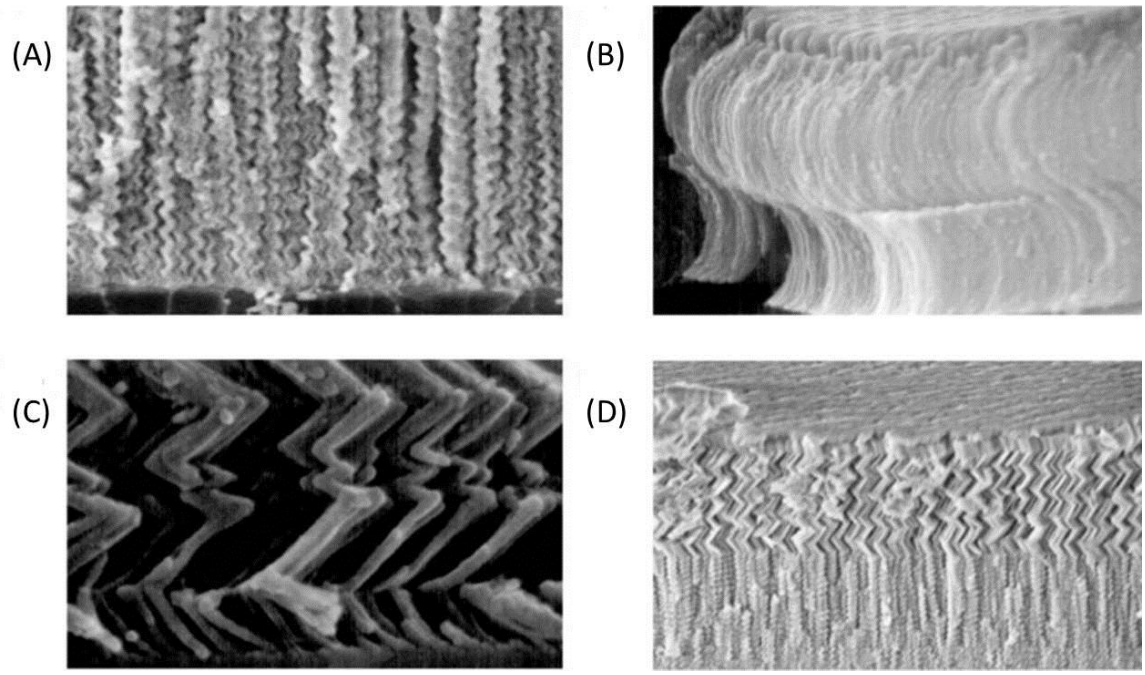


**Figure 1.5:** Examples of STFs: (A) a chiral STF, (B) and (C) sculptured nematic thin films, and (D) a hybrid STF [41].

Another method by which chiral STFs are fabricated is the serial bideposition (SBD) technique. This technique increases the local linear birefringence [42]. Sequential subdeposits are made either from two oppositely oriented sources or from a real source and one simulated by a 180° rotation of the substrate [43]. Once two subdeposits have been made, the substrate is incrementally rotated by a small angle $\Delta\xi$, and two new subdeposits are made, and so on. The incremental angle $\Delta\xi$ can be about 3° to 18° [43, 44], depending on the application.

When the collimated vapor flux is arriving obliquely onto the substrate from two opposite directions, anisotropic self-shadowing still exists. The average mass density of the film is higher than of STFs fabricated with just one vapor flux, since the second source deposits in the shadowed regions of the first deposit.

## 1.3 Optics of Chiral STFs

A chiral STF comprises helical nanocolumns with a pitch 2Ω, where Ω is the structural half-period. When light is normally incident on a chiral STF it exhibits the circular Bragg phenomenon over a range of wavelengths typically between 50 and 100 nm (called the circular Bragg regime). Within this regime, incident circularly polarized light of handedness matching the structural handedness of the film is highly reflected, while incident circularly polarized light of the opposite handedness is highly transmitted, provided the chiral STF is sufficiently thick [30].

Let a chiral STF occupy the region between planes $z = -L$ and $z = L$. The relative permittivity dyadic of the chiral STF can be written as

$$\underline{\underline{\varepsilon}}_r^{ChiralSTF}(z,\omega) = \underline{\underline{\hat{S}}}_z(h,\frac{z}{\Omega}) \bullet \underline{\underline{\hat{S}}}_y(\chi) \bullet \underline{\underline{\varepsilon}}_{ref}^{o}(\omega) \bullet \underline{\underline{\hat{S}}}_y^T(\chi) \bullet \underline{\underline{\hat{S}}}_z^T(h,\frac{z}{\Omega}), \tag{1.1}$$

where $\omega$ is the angular frequency,

$$\underline{\underline{\varepsilon}}_{ref}^{o}(\omega) = \varepsilon_a(\omega)\mathbf{u}_z\mathbf{u}_z + \varepsilon_b(\omega)\mathbf{u}_x\mathbf{u}_x + \varepsilon_c(\omega)\mathbf{u}_y\mathbf{u}_y \tag{1.2}$$

is the reference relative permittivity dyadic, and $\varepsilon_{a,b,c}$ are reference relative permittivity scalars which are $\omega$-dependent. The rotation dyadic that describes the rise of the helical nanocolumns with respect to the substrate plane is written as

$$\underline{\underline{\hat{S}}}_y(\chi) = \mathbf{u}_y\mathbf{u}_y + (\mathbf{u}_x\mathbf{u}_x + \mathbf{u}_z\mathbf{u}_z)\cos(\chi) + (\mathbf{u}_z\mathbf{u}_x - \mathbf{u}_x\mathbf{u}_z)\sin(\chi). \tag{1.3}$$

The other dyadic $\underline{\underline{\hat{S}}}_z\left(h, \frac{z}{\Omega}\right)$ in Eq. (1.1) describes the rotation about the $z$ axis and is written as

$$\underline{\underline{\hat{S}}}_z\left(h, \frac{z}{\Omega}\right) = \mathbf{u}_z\mathbf{u}_z + (\mathbf{u}_x\mathbf{u}_x + \mathbf{u}_y\mathbf{u}_y)\cos\left(h\frac{z}{\Omega}\right) + (\mathbf{u}_y\mathbf{u}_x - \mathbf{u}_x\mathbf{u}_y)\sin\left(h\frac{z}{\Omega}\right), \tag{1.4}$$

where the structural handedness parameter $h$ can equal +1 or -1, respectively, to indicate either a right-handed or a left-handed chiral STF. In Eqs (1.2) (1.4), $\mathbf{u}_x$, $\mathbf{u}_y$, and $\mathbf{u}_z$ are Cartesian unit vectors.

If the reference relative permittivity scalars of the chiral STF do not depend strongly on the angular frequency $\omega$ of the incident plane wave and the chiral STF is composed of materials with negligible losses, the central free-space wavelength of the circular Bragg regime is estimated as

$$\lambda_o^{Br} \cong \Omega\left(\sqrt{\varepsilon_c} + \sqrt{\varepsilon_d}\right), \tag{1.5}$$

where

$$\varepsilon_d = \varepsilon_a\varepsilon_b / \left(\varepsilon_a \cos^2\chi + \varepsilon_b \sin^2\chi\right)^{1/2} \tag{1.6}$$

is a composite relative permittivity scalar [30]. The full-wave-at-half-maximum bandwidth of the circular Bragg regime is estimated as

$$\Delta\lambda_o^{Br} = \left|\sqrt{\varepsilon_c} + \sqrt{\varepsilon_d}\right|. \tag{1.7}$$

Therefore, it is clear from Eqs. (1.5) and (1.6) that the central wavelength of the

circular Bragg regime $\lambda_o^{Br}$ is dependent on the helical pitch and the chosen material. However, the location of the central Bragg wavelength is also governed by the vapor flux angle $\chi_v$ which governs $\chi$, $\varepsilon_c$, and $\varepsilon_d$. Thus, Eq. (1.5) shows that the central Bragg wavelength $\lambda_o^{Br}$ can be chosen over a wide range of wavelengths, to accommodate specific applications, by a proper choice of the deposition parameters and the material to be evaporated.

## 1.4 Circular-polarization-independent Mirrors

There are two types of chiral STFs in which the discrimination between right-circular-polarized (RCP) light and left-circular-polarized (LCP) light is negligible. They are

(i) films which exhibit a psuedoisotropic point [45] and

(ii) films where the vapor flux angle $\chi_v$ varies during deposition [6].

### 1.4.1 Psuedoisotropic point in chiral STFs

For CTFs, the anisotropy arising from OAD implies that $\varepsilon_{a,b,c}$ are dependent on $\chi_v$. Hodgkinson *et al.* developed parametric relationships [46] to relate the relative permittivity scalars $\varepsilon_{a,b,c}$ and $\chi$ to deposition parameters.

These relationships are not universal and will vary from system to system, and even possibly over a period of time on a specific system. It is expected that similar relationships are applicable to chiral STFs since $\chi_v$ is held constant during deposition like a CTF. Lakhtakia predicted that a specific value of $\chi_v$ exists so that $\varepsilon_c = \varepsilon_d$ [45]. This value of $\chi_v$ is called the psuedoisotropic point $\chi_v^{Pi}$ where linear birefringence vanishes for

normally incident plane waves, and the chiral STF responds like an isotropic material to a normally incident plane wave of arbitrary polarization state. Therefore, the circular Bragg phenomenon can not exist [45] and an optical engineer will not be able to distinguish between RCP and LCP light.

### 1.4.2 Continuously modulated $\chi_v$ in chiral STFs

In the second case, theory [6] has shown that a chiral STF will exhibit the same reflectances and transmittances whether the normally incident plane wave is RCP or LCP, provided the vapor flux angle $\chi_v$ had been suitably varied during the fabrication of that chiral STF. Specifically, suppose that $\chi_v$ is sinusoidally modulated with a period equal to the helical pitch. With low rocking amplitudes, the circular Bragg phenomenon will still be exhibited. But, it is replaced with a Bragg phenomenon similar to that exhibited by a quarter-wave stack when the rocking amplitude is sufficiently large [6]. Polo and Lakhtakia described the sinusoidal modulation of $\chi_v$ as [6]

$$\chi_v(z) = \tilde{\chi}_v + \delta_v \sin(2N_{\mathrm{mod}} \frac{\pi z}{\Omega}), \tag{1.8}$$

where $\tilde{\chi}_v$ is the average value of $\chi_v$, $\delta_v$ is the rocking amplitude, and $N_{mod}$ is the number of oscillations over a structural half-period of the STF. The quantity $N_{mod}$ can be either an integer or a half integer.

Tilt-modulated chiral STFs should have two advantages over the quarter-wave stack for application as Bragg reflectors. First, a conventional quarter-wave stack is a multi-layer thin film which requires the alternating deposition of two different source materials in order to create the permittivity contrast between adjacent layers; however,

tilt-modulated chiral STFs only need one material [6]. This will save deposition time and reduce the cost of fabrication. Second, the range of wavelengths over which the quarter-wave stack acts as a reflector is governed by the difference in the relative permittivity scalars of its two constituent materials. Changing the layer thickness and/or selection of materials is required to engineer the bandwidth of the reflection/transmittance regime of the film [6]. For a tilt-modulated chiral STF, the bandwidth can be engineered simply by changing $\chi_v$. Therefore it is of interest to fabricate these tilt-modulated chiral STFs to replace conventional quarter-wave stacks.

## 1.5 Motivation for This Thesis

Although the characteristics of tilt-modulated chiral STFs have been theoretically predicted, no research efforts have been made to experimentally prove those predictions. Therefore, the objectives of this research endeavor were to (i) fabricate tilt-modulated chiral STFs by resistive-heating PVD, (ii) optically characterize the suppression of the circular Bragg phenomenon when a maximum rocking amplitude is reached, and (iii) verify the structural chirality of the film is maintained, even though the substrate is rocked during fabrication.

## 1.6 Outline of This Thesis

To achieve objective (i), zinc selenide was chosen as the dielectric material to be evaporated. The logic for choosing this material is based on its bulk properties that are presented in Chapter 2. A brief discussion on other areas of optics and electronics where ZnSe is used is also included. Chapter 3 provides a description of the fabrication of chiral

STFs with synchronous substrate rocking, starting with substrate preparation, methods for programming substrate-rotating motors, the thin-film deposition process, and the optical experiment used to verify the accomplishment of objective (ii).

Chapter 4 provides measured transmittance spectrums of tilt-modulated chiral STFs. These graphs show the gradual suppression of the circular Bragg phenomenon as the rocking amplitude increase. Chapter 4 also has SEM images displaying the morphology of these thin films which qualitatively verify the theoretical results of Polo and Lakhtakia, and ultimately achieving objective (iii).

A brief summary of all experimental results along with suggestions on future research concludes the thesis in Chapter 5.

# CHAPTER 2

# ZINC SELENIDE

The first step in fabricating tilt-modulated chiral STFs is to select an appropriate material to be evaporated and eventually deposited. The choice is based on the bulk properties of materials.

Zinc selenide (ZnSe) is an attractive choice for fabricating tilt-modulated chiral STFs due to its high refractive index, low sublimation point for fabricating thin films through thermal-evaporation techniques with ease, optical transparency over a wide range of wavelengths, and robustness [47]. Therefore, ZnSe was chosen to fabricate all the STFs used in experimental research reported in this thesis.

In this chapter, relevant physical properties of bulk ZnSe are discussed. A brief discussion of optical and electrical applications is also included.

## 2.1 ZnSe Material Properties

ZnSe is a direct-bandgap II-VI compound semiconductor that is composed of zinc (Group II) and selenium (Group VI). Structurally, ZnSe has the zincblende structure, that is, a face-centered cubic (FCC) crystalline structure [49]. At room temperature, the lattice constant of the unit cell in the FCC crystalline structure is 0.567 nm. The room-temperature melting point is 1520 °C due to highly covalent bonds, but ZnSe has been experimentally shown to sublime at approximately 660 °C in a low-pressure environment (~$10^{-5}$ Torr), which makes resistive-heating PVD a suitable technique for evaporating the

material [50].

The most attractive quality of ZnSe for fabricating tilt-modulated chiral STFs is its high refractive index which is ~ 2.7 in the visible regime [47]. The refractive index is predominantly real-valued (since dissipation is negligible) for $\lambda_o \in [458,2000]$ nm, which allows $\lambda_o^{Br}$ to be positioned anywhere in the visible and infrared spectral regimes. The relationship between the minimum wavelength where light is not absorbed and the bandgap of the material is

$$\lambda_{\min} = \frac{hc}{E_g}, \tag{2.1}$$

where $h$ is Planck's constant, $E_g$ is the bandgap energy, and $c$ is the free-space speed of light. As $E_g$ for ZnSe is 2.7 eV, $\lambda_{min}$ is in the blue region of the visible spectrum [50]. The appendix of this thesis has a list of relevant physical properties of ZnSe.

**2.2 Zinc-selenide applications**

Since ZnSe has a high refractive index and is a direct-bandgap semiconductor, it is a promising material for optics and optoelectronics. For example, its direct-bandgap feature has been exploited to fabricate blue-green laser diodes [51], light-emitting diodes [52], quantum dots [53], and beam splitters in mid-IR laser sources for remote sensing [54]. The high refractive index of ZnSe has been taken advantage of to fabricate dielectric mirrors [55], optically controlled switches [56], and optical waveguides [57].

# CHAPTER 3

# EXPERIMENTAL PROCEDURES

Once a material had been chosen for fabricating tilt-modulated chiral STFs, the resistive-heating PVD technique was employed to evaporate the material for thin-film deposition and an optical experiment was performed to characterize each film.

In this chapter, the steps for fabricating and characterizing a chiral STF with/without tilt-modulation are explained. The key steps for fabricating and characterizing these chiral STFs are (i) preparing the substrate for deposition, (ii) programming the stepper motors to rotate and/or tilt, (iii) evaporating the material and eventually depositing its vapor onto the rotating/rocking substrate, and (iv) characterizing the optical responses with an optical experiment.

## 3.1 Resistive-heating Physical Vapor Deposition

As different techniques for STF fabrication are discussed in Chapter 1, this section is focused on resistive-heating PVD employed for this thesis. This technique was chosen for three main reasons:

(i) The deposition system is readily available.

(ii) The deposition system has two pre-installed stepper motors necessary for substrate rotation and/or rocking.

(iii) The time to fabricate all STFs is significantly lower through resistive heating as opposed to the other technique implementable in the departmental facilities (i.e., EBPVD).

There are at least three advantages to using resistive-heating PVD. The evaporated atoms have a Maxwellian energy distribution, determined by the temperature of the source material, which reduces the number of high-speed adatoms that can cause deformation of the thin film being deposited. Also, the method provides a constant deposition rate and high purity.

Desirable thin films, whether they are sculptured or not, depend on certain parameters such as mass density, tooling factor, and z-ratio. Mass density depends upon the material one chooses to use to evaporate, and is 5.42 g $cm^{-3}$ for ZnSe [50].

A deposition controller calculates the deposition rate at the substrate plane using a pre-programmed tooling factor. The quartz crystal monitor (QCM) and the substrate are usually not located at the same distance from the source of the vapor flux. This difference is accounted for by a correction factor called the tooling factor. This is given by

$$Tooling\ \ Factor = \left( \frac{\Delta c}{\Delta s} \right)^2, \tag{3.1}$$

where $\Delta c$ is the distance from the source to the crystal and $\Delta s$ is the distance from the substrate to the source. The deposition rate measured by the QCM is multiplied by the tooling factor to obtain the correct deposition rate [58].

The z-ratio is used to adjust the changes in the resonant frequency of the crystal in the QCM. The correction is needed for the effects of acoustic-impedance mismatch between the source material and the crystal [58]. The z-ratio is the ratio of the acoustic impedance of the quartz crystal ($8.834 \times 10^5$ g $cm^{-2}$ $s^{-1}$) to that of the selected material.

The acoustic impedance of a material is the product of its mass density and the phase speed of acoustic waves in it. The z-ratio for ZnSe is 0.722.

### 3.2 Substrate Preparation

Substrate choice is important when depositing chiral STFs with/without synchronous substrate rocking. A planar, transmissive, and chemically inert substrate is desirable for STF growth. Therefore, Corning 7059® glass windows were used due to their high optical transmittance, flatness, good chemical resistance, and batch-to-batch consistency [81]. These commercially available glass windows are $5.08 \times 5.08$ cm$^2$ in size, and were cleaved with a diamond scribe into four $2.54 \times 2.54$ cm$^2$ substrates.

The glass windows are shipped pre-cleaned by the vendor, but needed to undergo significant cleaning prior to employment in order to (i) remove any suface-attached organic contaminants which could eventually damage the thin film integrity, (ii) reduce surface scattering, and (iii) promote adhesion.

Each substrate was placed in a Pyrex® glass dish, and underwent an ultrasonic cleaning in an acetone bath, an isopropyl alcohol (IPA) bath, and a deionized (DI) water bath, for ten minutes each in succession. After each cleaning step, the sample was rinsed with ultra-pure DI water and blow-dried with a nitrogen gun. The cleaned substrate was attached to a circular substrate holder with Kapton® tape which uniformly adheres to the substrate even at temperatures as high as 120 °C [60].

### 3.3 Material Loading and Back-end Processing

99.99% pure ZnSe in powder form was purchased from Alfa Aesar (Ward Hill, MA, USA). The material was placed in a tungsten boat purchased from Kurt J. Lesker Inc. (Clairton, PA, USA). Figure 3.1 shows ZnSe in granular form along with the boat used in the deposition experiments. A respirator was worn during material placement due to the extreme toxicity of ZnSe in powdered and evaporated forms.

The system was pumped down to a base pressure of $1.5 \times 10^{-5}$ Torr. This base pressure was reached before depositing any thin film for this work. While the vacuum system was pumping down, the program to control the stepper motors was written.

**Figure 3.1:** Notched boat employed in STF-deposition experiments and ZnSe in granular form [61, 62]

### 3.4 Deposition Process and Motor Programming

All chiral STFs fabricated were made to have a common pitch of $2\Omega$ = 330 nm and a maximum of 9 spatial periods resulting in approximately 3-μm-thick films. Two sets of films were fabricated: (i) one set with an average vapor flux angle $\tilde{\chi}_v$ of 20° and a rocking amplitude $\delta_v$ of 0°, 5°, 10°, and 15°; and (ii) another set with an average vapor

flux angle $\tilde{\chi}_v$ of 25° and rocking amplitudes of 0°, 5°, 10°, 15°, and 20°. For all tilt-modulated chiral STFs ($\delta_v \neq 0°$), the number $N_{mod}$ was set equal to 1.

I chose (i) $\tilde{\chi}_v = 20°$ for one set of films in order to place the circular Bragg phenomenon in the visible spectrum and (ii) $\tilde{\chi}_v = 25°$ for the second set of films in order to verify that $\lambda_o^{Br}$ of the circular Bragg phenomenon could be changed simply by changing $\tilde{\chi}_v$. The SBD technique used for fabricating chiral STFs (described in Section 1.2.2) was used to fabricate all thin films presented in this thesis.

### 3.4.1 Stepper motor programming

For fabricating chiral STFs without tilt modulation, the vapor flux angle $\chi_v$ has to be held constant throughout deposition. Therefore, the stepper motor which rotates the substrate about an axis tangential to the substrate plane was programmed to keep $\chi_v$ fixed at either 20° or 25°, depending on the film. A second stepper motor was programmed to rotate the substrate about the $z$ axis which passes normally through the center of the substrate. Step-wise rotation of this substrate gives rise to chiral morphology. The substrate holder was programmed to rotate 180° clockwise before one deposition, then wait for 2.91 s before a second clockwise rotation of 183°(ergo, $\Delta\xi$ of 3°) and a second deposition, thereby simulating a bideposition process. There are 120 steps required to complete one full rotation.

For tilt-modulated chiral STFs, programs to control the stepper motors were written similar to that for simple chiral STFs, but accounted for the substrate rocking motion.

One stepper motor was programmed to initially tilt the substrate about an axis tangential to the substrate plane to $\tilde{\chi}_v + \delta_v$. This motor then would gradually rock the substrate holder by 30 equal increments to $\tilde{\chi}_v - \delta_v$. The second stepper motor which rotates the substrate about the $z$ axis was programmed with the same parameters as for a chiral STF without tilt modulation (i.e., $\delta_v = 0°$). Then, the first motor was programmed to gradually rock the substrate by another 30 equal increments to $\chi_v + \delta_v$, and the second motor was programmed to rotate the substrate about the $z$ axis another half period. The rocking period and the rotation period were of the same duration. Figure 3.2 shows a schematic of the substrate holder which rotated and/or tilted the substrate used to fabricate all thin films fabricated for the work reported in this thesis**.**

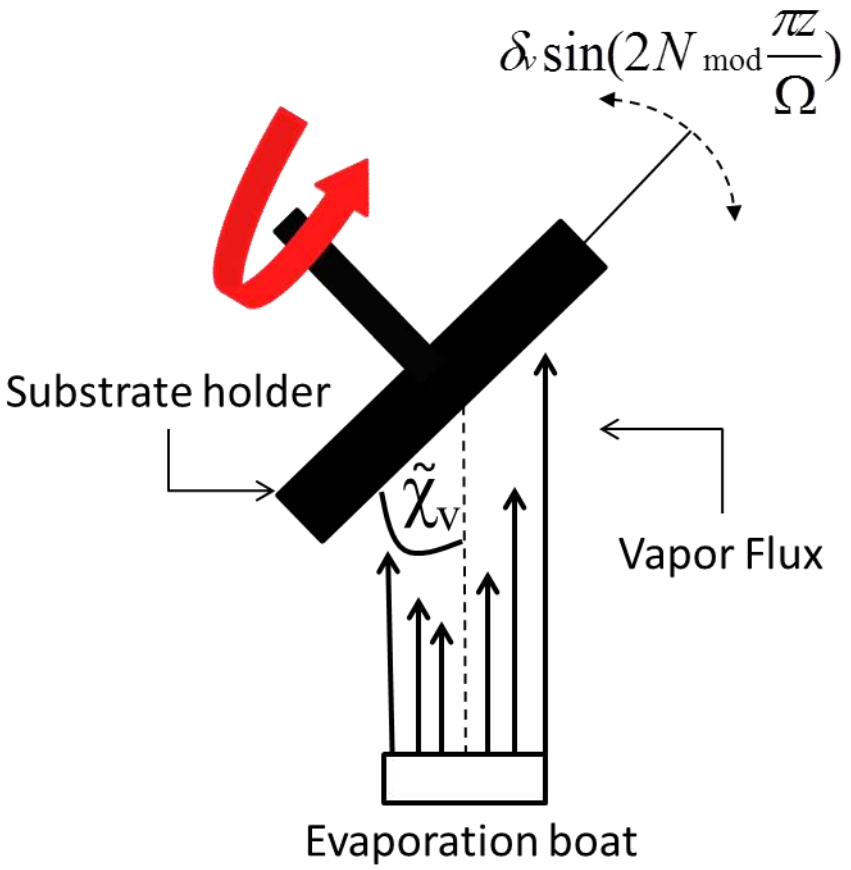


**Figure 3.2:** Schematic of the substrate holder programmed for a sinusoidally varying vapor flux angle with an average $\tilde{\chi}_v$, maximum $\tilde{\chi}_v + \delta_v$, and minimum $\tilde{\chi}_v - \delta_v$.

### 3.4.2 Deposition process

A program was chosen and uploaded to a computer which controls the substrate motors once the base pressure was reached. The mass density of ZnSe and tooling factor were programmed into the deposition controller. The mass density of ZnSe is 5.42 g cm$^{-3}$. The tooling factor for $\tilde{\chi}_v = 20°$ is 153, whereas it is 162 for $\tilde{\chi}_v = 25°$.

A current was passed though the boat to resistively heat the source material in increments of 5 A to stabilize the voltage readout on the current source. At approximately 90 A, the majority of the ZnSe sintered in the boat, and the shutter was opened with the stepper motors operating so that a vapor flux could be incident on the substrate.

A deposition rate of 0.4 nm $s^{-1}$, which quantifies the amount of vapor flux arriving at a location per unit time, was measured *in situ* by the QCM. As the deposition rate changes, the material depletes in the boat and the vapor pressure first increases and then slowly decreases to the base pressure. A variation of 0.02 nm $s^{-1}$ in the deposition was deemed acceptable.

Due to the small capacity of the boat to hold the source material and the power limitations of the deposition system, two sequential depositions must be made to deposit a 9-spatial-period-thick film. When the QCM would indicate that the thickness of the film was 1500 nm, the substrate motors would be paused, the shutter would be closed, and the evaporation chamber would be opened to refill the tungsten boat with more ZnSe. A second deposition of 1500 nm after resuming substrate rotation was made, once the chamber again reached a base pressure of $1.5 \times 10^{-5}$ Torr, which ultimately led to a 3-μm-thick film. This two-step deposition process has not been reported for making chiral STFs.

## 3.5 Optical Setup and Data Collection

An optical experiment to collect the circular and linear transmittance spectrums was carried out after the fabrication of a film. Transmittances were measured instead of

reflectances because all theoretical predictions on tilt-modulated chiral STFs were based on normally incident light.

### 3.5.1 Optical setup

Unpolarized light from a white-light source was passed normally through a linear polarizer, two Fresnel rhombs, and again through another linear polarizer before being detected by a detector. The sample was placed between the two Fresnel rhombs. If both the linear polarizers are rotated by 45° (or -45°), the plane wave is LCP (or RCP). A (i) Leica 100 W halogen bulb white-light source, (ii) two Glan-Thompson linear polarizers, (iii) two quarter-wave Fresnel rhombs, (iv) and a silicon-based optical fiber leading to a spectrometer were the optical components of the setup used for all optical experiments reported in this thesis. The setup is schematically shown in Figure 3.3.

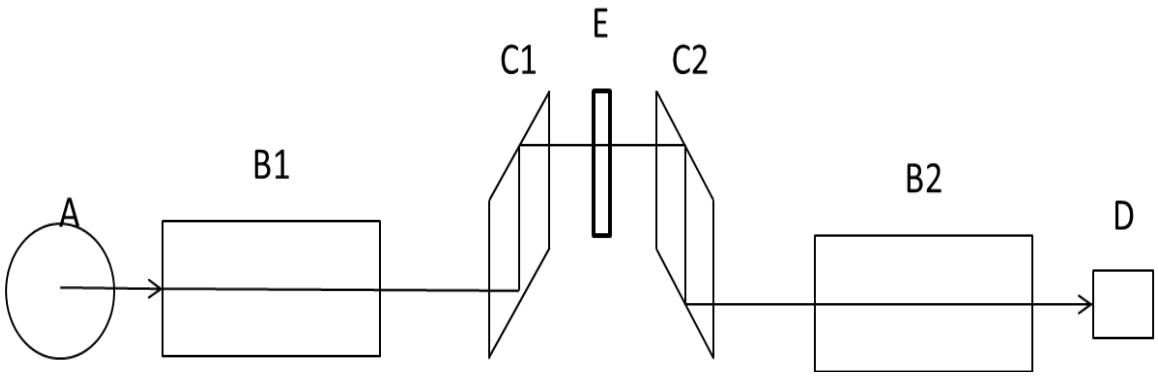


**Figure 3.3:** Schematic of the beam path for measuring transmittances of chiral STFs: (A) light source; (B1) first Glan-Thompson linear polarizer; (C1) first Fresnel rhomb; (E) substrate holder with sample positioned such that the beam passes through it; (C2) second Fresnel rhomb; (B2) second Glan-Thompson linear polarizer; and (D) Fiber-optic cable connected to a HR2000 OceanOptics® spectrometer.

The plane wave leaving the first Fresnel rhomb is circularly polarized with handedness based on the rotation of the first linear polarizer. The plane wave is normally incident onto a thin film/substrate/substrate-holder stack when looking from the light source. The transmitted wave then propagates to the second Fresnel rhomb, and to the second linear polarizer. A silicon-based optical fiber leading to an OceanOptics® HR2000 UV-VIR-NIR spectrometer was positioned perpendicularly onto the second linear polarizer in order to collect the light reaching the detector.

In order to determine linear transmittances, the Fresnel rhombs were removed from the beam path, and the linear polarizers were set to + 90° (or -90°) for p- (or s- ) polarization states.

### 3.5.2 Data collection

The transmittances for circularly polarized light are denoted as $T_{RR}$, $T_{LL}$, $T_{RL}$, and $T_{LR}$, and the transmittances for linearly polarized light are donoted as $T_{PP}$, $T_{SS}$, $T_{PS}$, and $T_{SP}$ in the remainder of this thesis. The second subscript denotes the polarization state of the light on the thin film, and the first one denotes the of polarization state of the detected light. For example, $T_{RL}$ denotes the portion of the incident power density transmitted as an RCP wave when the incident plane wave is LCP.

The procedure for obtaining the transmittances of each film is exemplified through $T_{RL}$ as follows:

(i) turn on the Leica 100 W halogen light source in a dark room under ambient conditions, and allow it to stabilize for 30 minutes;

(ii) rotate the first Glan-Thompson linear polarizers (B1 in Figure 3.3) to -45° and the rotate the second (B2) to +45°;

(iii) maximize the light intensity collected by the detector without going into saturation without the film in the film holder, by adjusting the voltage on the light source;

(iv) capture this intensity profile and store it as $a_R$;

(v) remove the sample and block beam path;

(vi) capture the intensity profile (essentially zero intensity in a.u.), and label this profile as '*Dark*';

(vii) secure a film into the film holder, allow normally incident light to transmit through the film, and capture the transmitted intensity profile. Store this and save it as $T_{RL\ measured}$; and

(viii) calculate the transmittance $T_{RL}$ using the equation provided in Table 3.1.

Let me note that each film's transmittances were measured within one day of fabrication.

**Table 3.1** Equations to calculate the transmittances for circularly polarized (column A) and linearly polarized incident light (column B) from experimental data.

| (A) | (B) |
|---|---|
| $T_{RR} = \left( \frac{T_{RR\,measured} - Dark}{a_R - Dark} \right)$ | $T_{PP} = \left( \frac{T_{PP_{measured}} - Dark}{a_P - Dark} \right)$ |
| $T_{LL} = \left( \frac{T_{LL\,measured} - Dark}{a_L - Dark} \right)$ | $T_{SS} = \left( \frac{T_{SS_{measured}} - Dark}{a_S - Dark} \right)$ |
| $T_{RL} = \left( \frac{T_{RL\,measured} - Dark}{a_R - Dark} \right)$ | $T_{PS} = \left( \frac{T_{PS_{measured}} - Dark}{a_P - Dark} \right)$ |
| $T_{LR} = \left( \frac{T_{LR\,measured} - Dark}{a_L - Dark} \right)$ | $T_{SP} = \left( \frac{T_{SP_{measured}} - Dark}{a_S - Dark} \right)$ |
| $a_R$ - Amplitude of incident RCP plane wave | $a_P$ - Amplitude of incident p-polarized plane wave |
| $a_L$ - Amplitude of incident LCP plane wave | $a_S$ - Amplitude of incident s-polarized plane wave |

# CHAPTER 4

# RESULTS OF OPTICAL EXPERIMENTS AND THIN-FILM MORPHOLOGY

In this chapter, spectrums of the transmittances for linearly and circularly polarized plane waves normally incident on chiral STFs with/without tilt-modulation are presented. For normally incident circularly polarized plane waves, the suppression of the Bragg phenomenon is observed when a maximum rocking amplitude is reached. SEM images of chiral STFs and tilt-modulated chiral STFs are also presented, which exhibit chiral, non-homogeneous, and periodic morphology, even though the substrate was rocked about an axis tangential to the substrate plane.

## 4.1 Circular Transmittance Spectrums for $\tilde{\chi}_v = 20°$

The measured circular transmittances of a structurally right-handed chiral STF, for which $\tilde{\chi}_v = 20°$ was set, are shown in Figure 4.1(A). As can be concluded from this figure, an LCP plane wave is moderately transmitted for normal incidence over the range of wavelengths $600 \leq \lambda_o \leq 675$ nm, which is the circular Bragg regime. The moderately high values of $T_{LL}$ within the circular Bragg regime indicate that an incident LCP plane wave maintains its polarization state in transmission. An incident RCP plane wave is highly reflected within the same spectral regime. The central wavelength $\lambda_o^{Br}$ of the circular Bragg regime is approximately 650 nm, and the difference between $T_{LL}$ and $T_{RR}$ is 0.43 at that wavelength.

Figures 4.1 (B) – (D) are circular-transmittance spectrums for $\tilde{\chi}_v = 20°$, and (B) $\delta_v = 5°$, (C) $\delta_v = 10°$, and (D) $\delta_v = 15°$. Each figure clearly shows the Bragg phenomenon, but as the rocking amplitude $\delta_v$ reaches a maximum of 15°, the discrimination between incident RCP and LCP light at $\lambda_o^{Br}$ is greatly reduced. The difference between $T_{RR}$ and $T_{LL}$ light at $\lambda_o^{Br}$ in Figures 4.1 (B), (C), and (D) diminishes to 0.42, 0.40, and 0.07, respectively. Therefore, when a maximum rocking amplitude is reached, the tilt-modulated chiral STF is almost completely insensitive to the polarization state of the normally incident wave, although a Bragg phenomenon remains. Also, the cross-polarized circular transmittances are almost non-existent over the circular Bragg regime.

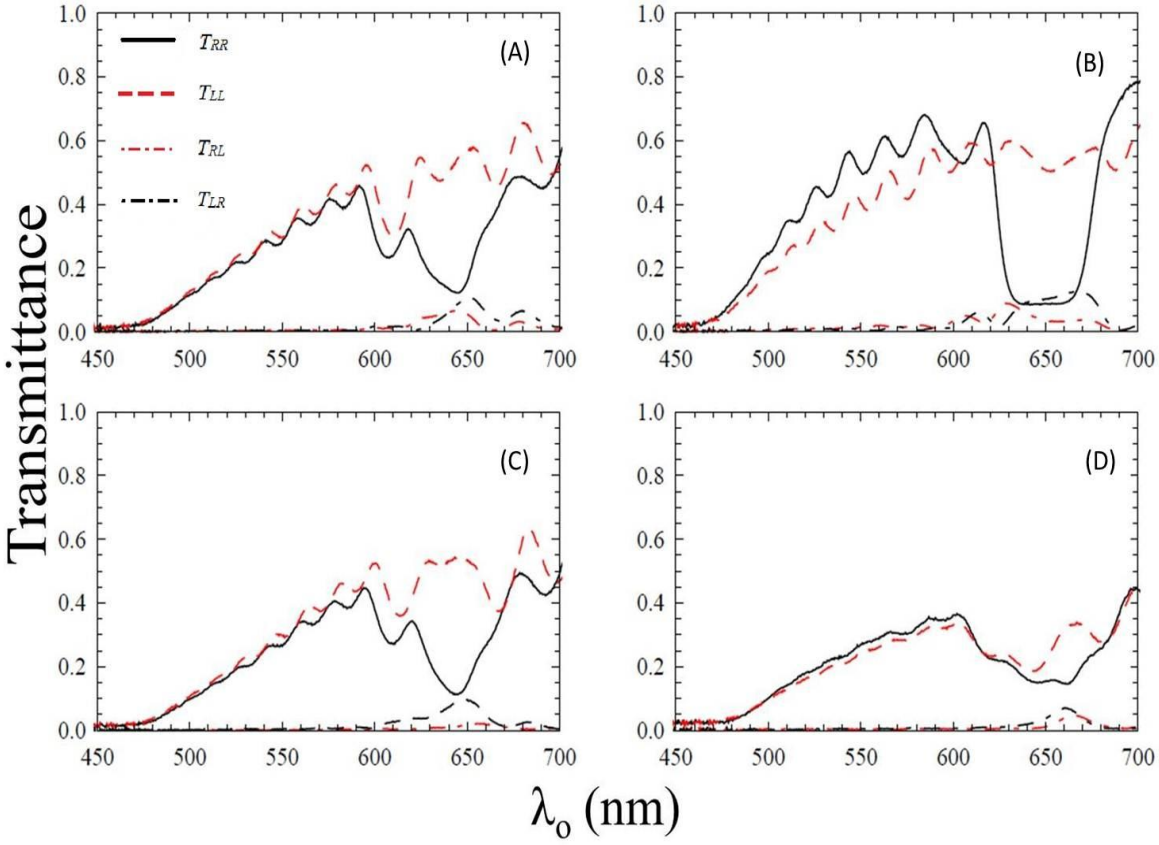


**Figure 4.1:** Circular transmittance spectrums of a chiral STF fabricated with $\tilde{\chi}_v = 20°$ with/without rocking motion: (A) $\delta_v = 0°$, (B) $\delta_v = 5°$, (C) $\delta_v = 10°$, and (D) $\delta_v = 15°$.

## 4.2 Linear Transmittance Spectrums for $\tilde{\chi}_v = 20°$

Figures 4.2 (A) – (D) show the measured linear transmittance spectrums for $\tilde{\chi}_v$ = 20°. An incident p-polarized plane wave is transmitted more than an s-polarized plane wave, as seen in Figure 4.2 (A). Similar to the circular transmittances, the bandwidth of the Bragg regime is ($600 \leq \lambda_o \leq 675$ nm) is still evident. In Figures 4.2 (B) – (D), the curves of $T_{SS}$ and $T_{PP}$ begin to take the same form with little discrimination at $\lambda_o^{Br}$ and in the Bragg regime, as $\delta_v$ increases. At $\lambda_o^{Br}$, the difference between $T_{SS}$ and $T_{PP}$ is ~ 0.1 in Figure 4.2 (D).

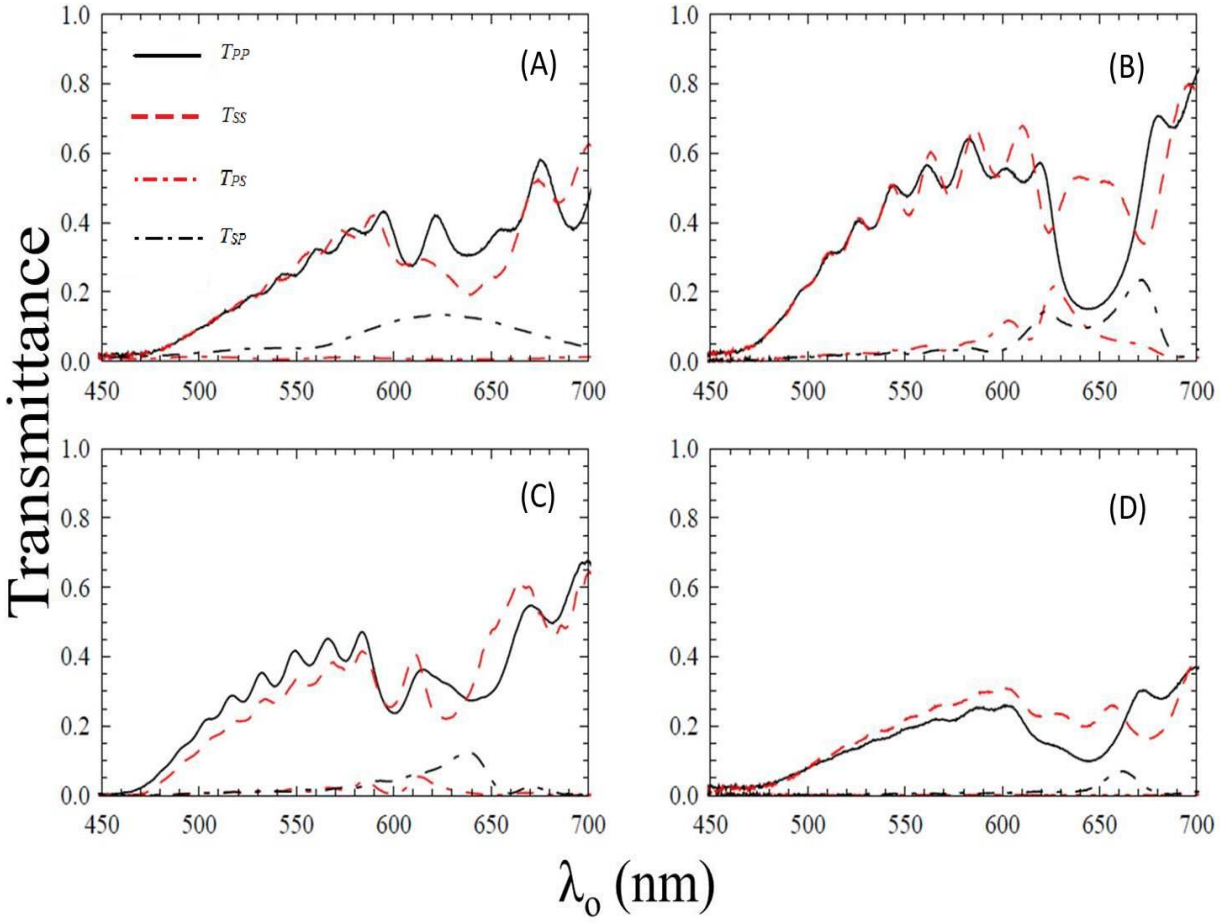


**Figure 4.2:** Linear transmittance spectrums of a chiral STF fabricated with $\tilde{\chi}_v = 20°$ with/without rocking motion: (A) $\delta_v = 0°$, (B) $\delta_v = 5°$, (C) $\delta_v = 10°$, and (D) $\delta_v = 15°$.

## 4.3 Circular Transmittance Spectrums for $\tilde{\chi}_v = 25°$

A second set of simple and tilt-modulated chiral STFs with $\tilde{\chi}_v = 25°$ was fabricated and characterized to verify that the bandwidth of the circular Bragg phenomenon can be changed simply by changing $\tilde{\chi}_v$. Figures 4.3 (A) – (E) present the spectrums of circular transmittances for $\tilde{\chi}_v = 25°$. Figures 4.3 (B), (C), (D), and (E) are for tilt-modulated chiral STFs where $\delta_v = 5°$, 10°, 15°, and 20°, respectively.

In Figure 4.3 (A), an incident LCP plane wave is highly transmitted whereas an incident RCP plane wave is highly reflected in the circular Bragg regime $725 \leq \lambda_o \leq 825$ nm. A low $T_{RR}$ is consistent with a right-handed structurally chiral STF. The central Bragg wavelength $\lambda_o^{Br}$ = 765 nm has red-shifted to the near-IR spectral regime. The circular Bragg phenomenon is better defined in Figure 4.3 (A) than in Figure 4.1 (A). There is a difference of 0.63 between $T_{RR}$ and $T_{LL}$ at $\lambda_o^{Br}$ in Figure 4.3 (A).

Figure 4.3 (B) shows that the circular Bragg regime has blue-shifted to $700 \leq \lambda_o \leq 800$ nm, whereas $\lambda_o^{Br}$ is approximately 730 nm. This shift can be attributed to modulating the vapor flux angle during fabrication. This spectrum still shows a strong circular Bragg phenomenon. The difference in $T_{RR}$ and $T_{LL}$ at $\lambda_o^{Br}$ has reduced to 0.51.

For $\delta_v$ = 10° (Figure 4.3 (C)), the circular Bragg phenomenon is still located at $700 \leq \lambda_o \leq 800$ nm and $\lambda_o^{Br}$ does not appear to have shifted. However, the spectrum of $T_{LL}$ is beginning to take the same shape as the spectrum of $T_{RR}$, whereas the difference between $T_{RR}$ and $T_{LL}$ is further reduced to 0.43 at $\lambda_o^{Br}$ . This suggests that the circular Bragg phenomenon is gradually reducing.

When the rocking amplitude is increased to $\delta_v$ = 15° (Figure 4.3 (D)), and then $\delta_v$ = 20° (Figure 4.3 (E)), the circular Bragg regime is red-shifted to $675 \leq \lambda_o \leq 750$ nm and $700 \leq \lambda_o \leq 775$ nm respectively. This has to be due to high values of $\delta_v$. When $\delta_v$ = 15°, the discrimination between $T_{RR}$ and $T_{LL}$ has reduced to 0.08 at $\lambda_o^{Br}$, and the difference is non-existent at $\lambda_o^{Br}$ for $\delta_v$ = 15°.

It is important to note that Figure 4.3 (E) displays the possibility of a twist-defect, which is a purposely inserted defect, caused by abruptly rotating the substrate 90° after depositing a a chiral STF [59,90]. A twist-defect would appear as a transmittance peak at $\lambda_o^{Br}$ with a bandwidth of approximately 10 nm. This is a possibility since the film was deposited in two steps; but that defect is not clearly evident in the SEM images presented in Section 4.5.

The circular transmittance spectrums in Figures 4.3 (A)-(E) suggest that suppression of the circular Bragg phenomenon is more pronounced for higher values of $\tilde{\chi}_v$ when compared to lower values of $\tilde{\chi}_v$. Futhermore, the transmittances in Figure confirm that a tilt-modulated chiral STF can behave similarly to a dielectric mirror, and that its bandwidth can be changed simply by changing $\tilde{\chi}_v$.

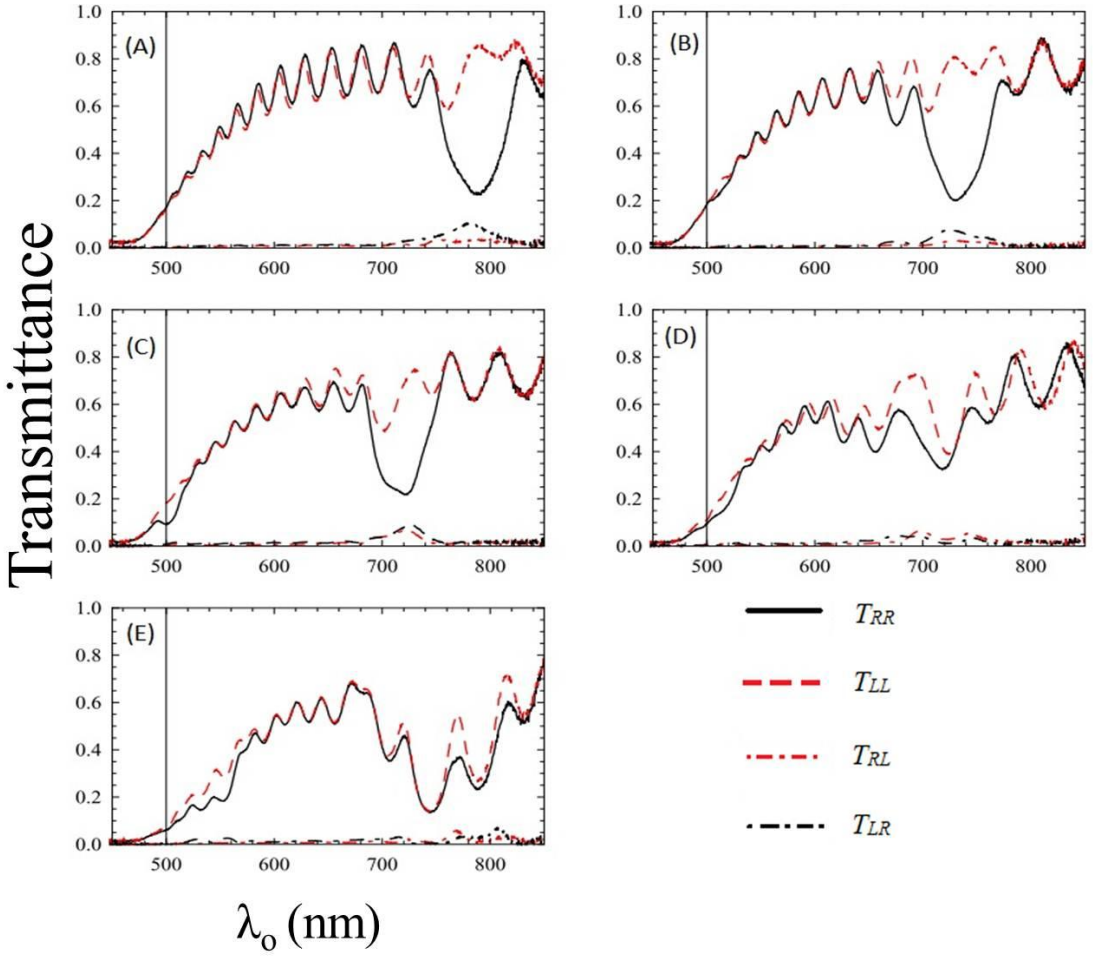


**Figures 4.3:** Circular transmittance spectrums of a chiral STF fabricated with $\tilde{\chi}_v = 25°$ with/without rocking motion: (A) $\delta_v = 0°$, (B) $\delta_v = 5°$, (C) $\delta_v = 10°$, (D) $\delta_v = 15°$, and (E) $\delta_v = 20°$.

## 4.4 Linear Transmittance Spectrums for $\tilde{\chi}_v = 25°$

Figure 4.4 shows the spectrums of linear transmittances for $\tilde{\chi}_v = 25°$. There is some discrimination between incident s-polarized and p-polarized plane waves, but this discrimination appears to reduce as $\delta_v$ increases. In Figure 4.4 (A), $T_{PP}$ is higher than $T_{SS}$ within the same circular Bragg regime as that of Figure 4.3 (A). In Figures 4.4 (B) – (E), the discrimination between incident s- and p-polarized plane waves is gradually reduced, and cross-polarization transmittances become virtually null within the Bragg regime. Figure 4.4 (E) also shows that the discrimination between an incident s-polarized plane wave and an incident p-polarized plane wave has reduced further to 0.06 at $\lambda_o^{Br}$ when compared to those for $\tilde{\chi}_v = 20°$ ($T_{PP} - T_{SS} \sim 0.1$ at $\lambda_o^{Br}$), which suggests that the plane-wave discrimination in linear transmittance is lower for higher values of $\tilde{\chi}_v$.

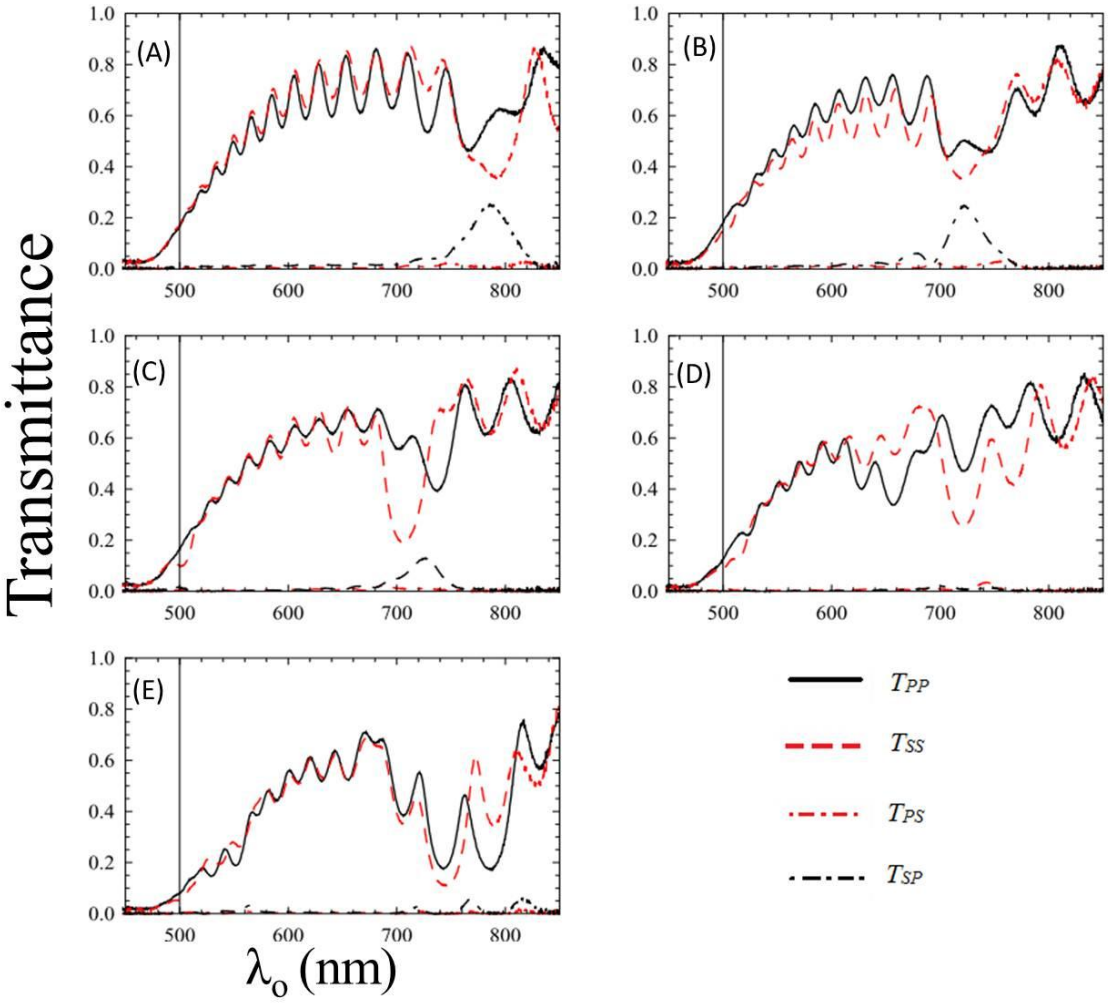


**Figure 4.4:** Linear transmittance spectrums of a chiral STF fabricated with $\tilde{\chi}_v = 25°$ with/without rocking motion: (A) $\delta_v = 0°$, (B) $\delta_v = 5°$, (C) $\delta_v = 10°$, (D) $\delta_v = 15°$, and (E) $\delta_v = 20°$.

### 4.5 Thin-film Morphology of Chiral and Tilt-modulated Chiral STFs

Field-emission scanning-electron-microscopy (FE-SEM) was used to image the morphology of chiral STFs and tilt-modulated chiral STFs. In this section, five images displaying the cross-sectional morphology of $\tilde{\chi}_v = 25°$ and $\delta_v = 0°$, 5°, 10°, 15°, and 20° on glass substrates are presented.

Sample preparation is crucial for imaging cross-sections of STFs. Due to the sample-size limitations of the FE-SEM tool, sample of size $2.54 \times 2.54$ cm$^2$ must be reduced to about $0.1 \times 0.1$ cm$^2$. One must be careful not to disturb the structural integrity of the film when reducing each sample to smaller pieces; therefore, one cannot simply use a diamond scribe to cleave the sample to a smaller size.

In order to overcome this challenge, the "freeze-fracturing" method [64] was adopted to reduce each sample to a smaller size. The sample was (i) placed into a plastic container, (ii) immersed in liquid nitrogen, and (iii) broken with a hammer and punch. The liquid nitrogen froze the entire sample and helped maintain the structural integrity of the thin film.

A reduced-sized sample was chosen and an ultra-thin film (~ 5 nm) of gold was sputtered onto the cross-section to make the sample conductive, which is required for FE-SEM imaging. Finally, the sample was positioned onto a sample holder with conductive tape before being placed in the FE-SEM chamber.

Figures 4.5 (A) and (B) are FE-SEM images of a sample for $\tilde{\chi}_v = 25°$ and $\delta_v = 0°$. This is a simple chiral STF displaying periodic, non-homogeneous, and chiral morphology. Figure 4.5 (A) is a low-resolution image. Measurements are included in this image to show that the chiral STF has an average thickness of 3.08 μm. This value is in good agreement with a QCM-reported thickness of 3.00 μm. Furthermore, these data verify that the *in-situ* QCM is properly reading the film thicknesses based on the deposition rate and tooling factor.

Image (B) is a high-resolution image of the same image. The extreme black and white contrasts in Figure 4.5(B) are due to charging effects on the glass substrate in which each image was taken. This phenomenon can be eliminated by depositing the chiral STF on a conductive medium, such as silicon, for SEM imaging.

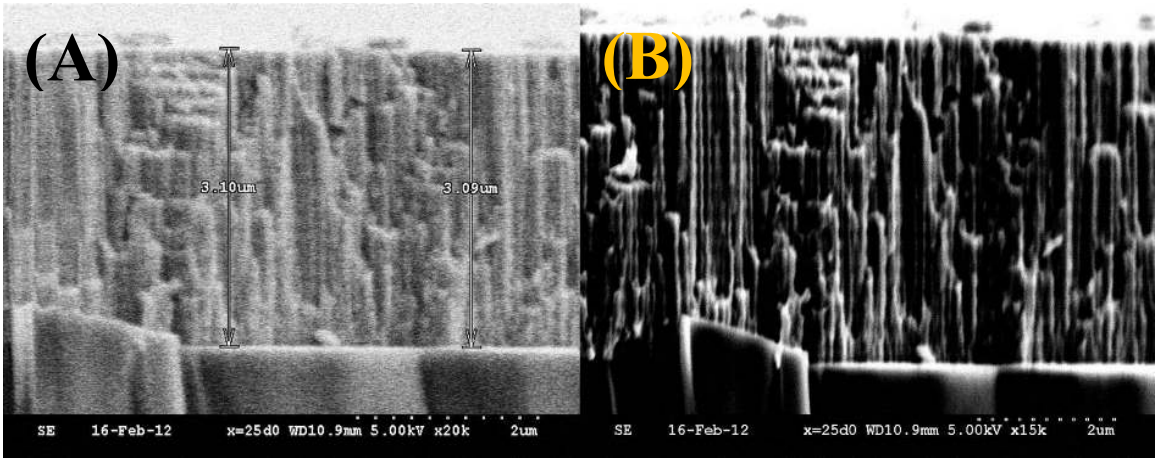


**Figure 4.5:** FE-SEM images of a chiral STF for which $\tilde{\chi}_v = 25°$ and $\delta_v = 0°$: (A) low-resolution image with thickness measurements, and (B) high-resolution image of the chiral STF.

Figures 4.6 (A) and (B) are FE-SEM images of a tilt-modulated chiral STF for which $\tilde{\chi}_v = 25°$ and $\delta_v = 5°$. Figure 4.6 (A) shows the average film thickness to be 3.04 μm. Figure 4.6 (B) is a high-resolution FE-SEM image which displays upright, parallel, non-homogeneous, and undoubtedly, chiral morphology. It is clearly seen in these images that structural chirality is maintained even though the substrate is rocked during deposition.

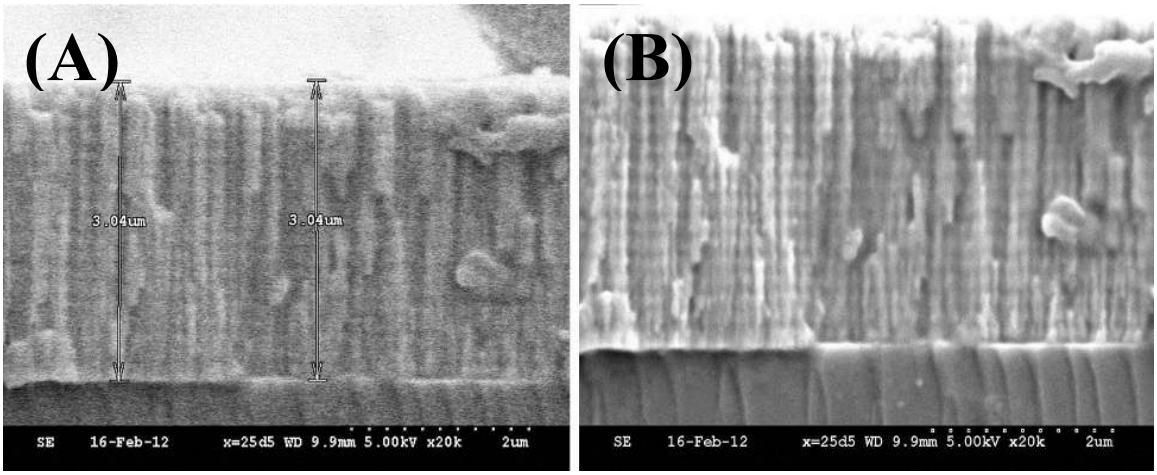


**Figure 4.6:** FE-SEM images of a chiral STF for which $\tilde{\chi}_v = 25°$ and $\delta_v = 5°$: (A) low-resolution image with thickness measurements, and (B) high-resolution image of the chiral STF.

Figures 4.7 (A) and (B) are FE-SEM images of a tilt-modulated chiral STF for which $\tilde{\chi}_v = 25°$ and $\delta_v = 10°$. Figure 4.7 (A) shows the average film thickness to be 3.08 μm. Figure 4.7 (B) is a high-resolution FE-SEM image which continues to display upright, parallel, non-homogeneous, and again, chiral morphology. However, Figure 4.7

(B) begins to show the chirality of the film being "stretched" along the thickness direction, which could be attributed to the moderate level of tilt modulation.

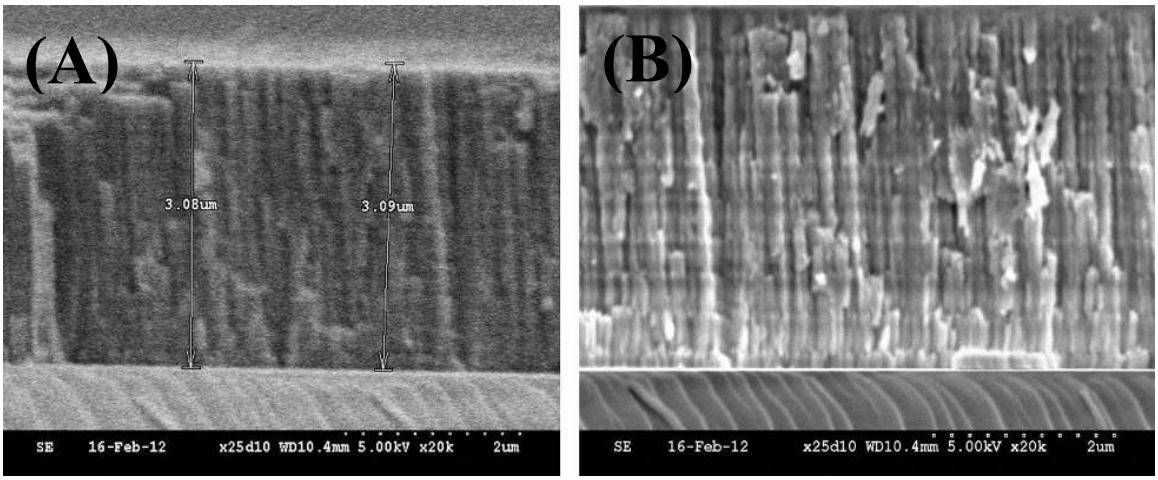


**Figure 4.7:** FE-SEM images of a chiral STF for which $\tilde{\chi}_v$ = 25° and $\delta_v$ = 10°: (A) low-resolution image with thickness measurements, and (B) high-resolution image of the chiral STF.

Figures 4.8 (A) and (B) are FE-SEM images of a tilt-modulated chiral STF for which $\tilde{\chi}_v$ = 25° and $\delta_v$ = 15°. Figure 4.8 (A) shows the average film thickness to be ~ 2.84 μm. This is in good agreement with the thickness of 2.89 μm read by the QCM. This film is thinner than the films in Figures 4.5 – 4.7 because the source material was totally depleted during growth, which was indicated during the fabrication by an unstable deposition rate. Therefore, the deposition process was stopped at 2.89 μm thickness in order to maintain the quality of the film. Figure 4.8 (B) is a high-resolution FE-SEM image which still exhibits upright, parallel, non-homogeneous, and chiral morphology. However, Figure 4.8 (B) shows the chirality of the helices to be futher stretched, which

can be due to more tilt modulation. Furthermore, this image clearly shows the structural period of the helices, which is typically unseen in SBD deposited filims.

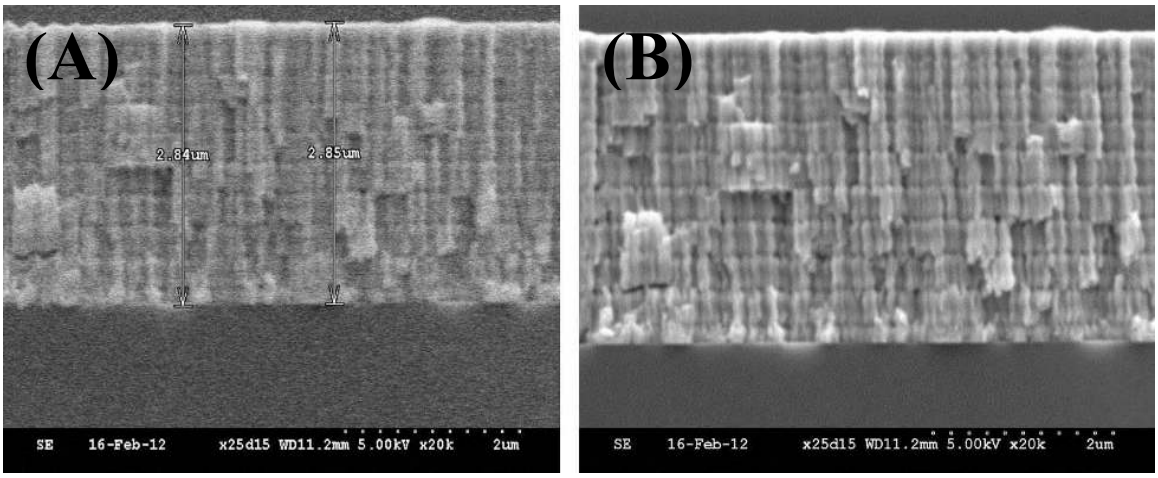


**Figure 4.8:** FE-SEM images of a chiral STF for which $\tilde{\chi}_v$ = 25° and $\delta_v$ = 15°: (A) low-resolution image with thickness measurements, and (B) high-resolution image of the chiral STF.

Figures 4.9 (A) and (B) are FE-SEM images of STF for which $\tilde{\chi}_v$ = 25° and $\delta_v$ = 20°. Figure 4.9 (A) shows the average film thickness to be ~ 3.24 μm. This is in good agreement with the thickness read by the QCM which was 3.10 μm. Figure 4.8 (B) is a high-resolution FE-SEM image. This image clearly shows upright, non-homogeneous, and parallel columns. However, the "stretching" along the thickness direction as seen in Figures 4.7 and 4.8 is so high that the film appears at first glance to have lost its structural chirality. In fact, the morphology suggests that each nanocolumn appears to be a 3-D nano-ribbon with twists. Lastly, Figure 4.9 (B) does not show any indication of a twist

defect, as discussed in Section 4.3.

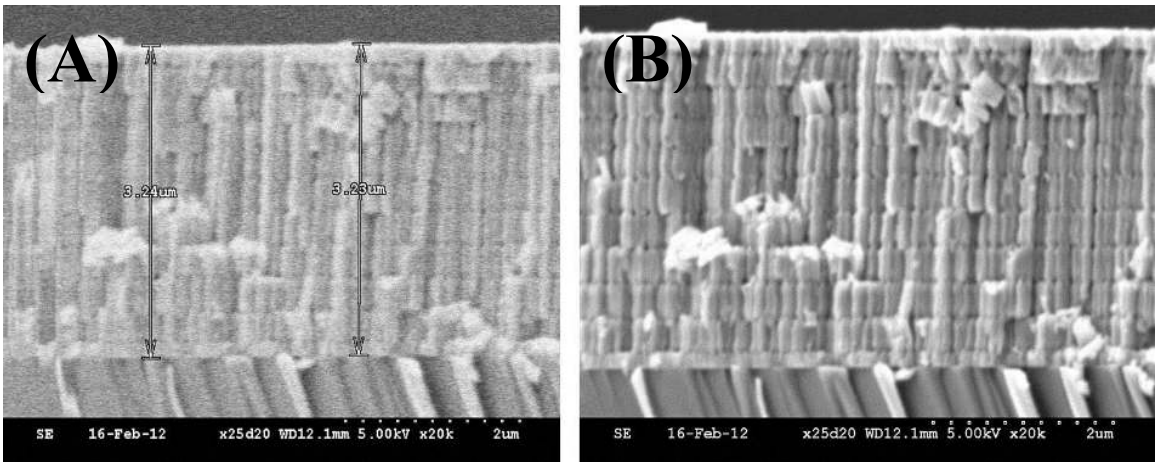


**Figure 4.9:** FE-SEM images of a chiral STF for which $\tilde{\chi}_v$ = 25° and $\delta_v$ = 20°: (A) low-resolution image with thickness measurements, and (B) high-resolution image of the chiral STF.

The theory for tilt-modulated chiral STFs states that as $\delta_v$ increases, the difference $T_{LL}$-$T_{RR}$ goes to zero, but the Bragg regime remains. The experimental work presented in this thesis shows that as $\delta_v$ increases, the difference $T_{LL}$-$T_{RR}$ decreases, and the Bragg regime still remains. However, perfect correspondence between the theory and this experiment is not obtained.

The theory used $\varepsilon_a$, $\varepsilon_b$, $\varepsilon_c$, and $\chi$ to $\chi_v$ relationships for a CTF [6]. CTF growth is static such that the vapor flux angle is held constant during deposition. These equations perhaps can be used for a chiral STF for which $\delta_v$ = 0°, but when there is rotation, the tilt angle changes dynamically. Between the relationship between $\chi$ and $\chi_v$ for a CTF and that for an SNTF [31] (rocking, but no rotation), it is known that there is a big difference [33].

This is the reason why qualitative agreement was obtained here with the theoretical predictions of Polo and Lakhtakia [6], but not anything close to a quantitative agreement.

# CHAPTER 5

# CONCLUSIONS AND FUTURE WORK

## 5.1 Conclusions

As was discussed in Chapter 1, the objectives of the work presented in this thesis were to (i) fabricate tilt-modulated chiral STFs by resistive-heating PVD, (ii) optically characterize the suppression of the circular Bragg phenomenon when a maximum rocking amplitude is reached, and (iii) verify the structural chirality of the film is maintained, even though the substrate is rocked during fabrication.

In order to achieve the first objective, ZnSe was chosen to fabricate chiral STFs and tilt-modulated chiral STFs on a glass substrate. ZnSe was an adequate choice due to its high refractive index, low sublimation point, optical transparency over a wide range of waelengths, and robustness.

The resistive-heating PVD technique was chosen for the deposition because the deposition system that was used (i) had pre-installed stepper motors which is necessary for substrate rotation and/or rocking, (ii) was readily available, and (iii) required less time to fabricate thin films as opposed to other techniques implementable in the university facilities. Also, resistive-heating PVD allows constant deposition rates and produces high-purity thin films.

Two sets of chiral STFs and tilt-modulated chiral STFs were fabricated by the SBD technique. Two computer-controlled stepper motors – one which tilts the substrate about an axis tangential to the substrate plane, and one that rotates the substrate about the

*z* axis which passes normally through the substrate – were programmed to have a desired tilt amplitude and rotation of the substrate. Both sets of chiral STFs differed only in the value of the average vapor flux angle $\tilde{\chi}_v$, and both sets comprised at least four types of chiral STFs with different values of tilt amplitude $\delta_v$, thereby achieving the first objective.

To achieve the second objective, the experimentally measured transmittances for both incident linearly and incident circularly polarized plane waves were obtained as functions of the free-space wavelength. Only, normally incident plane waves were considered. For circularly polarized plane waves, it was obsereved that the circular Bragg phenomenon was gradually suppressed over the Bragg regime as $\delta_v$ was increased. This observation was made for both sets of chiral STFs (with different values of $\tilde{\chi}_v$). However, the set of chiral STFs with the higher value of $\tilde{\chi}_v$ showed better suppression of the circular Bragg phenomenon than the one with the lower value of $\tilde{\chi}_v$. For linearly polarized plane waves, a similar phenomenon was observed where the discrimination between two linear-polarization states becomes less significant when the value of $\delta_v$ increases. Moreover, the discrimination between the two plane waves was found to be lower for a higher value of $\tilde{\chi}_v$ than for lower value of $\tilde{\chi}_v$.

In order to achieve the third objective, field-emission scanning-electron-microscopy was used to image the simple chiral STFs and tilt-modulated chiral STFs with a higher value of $\tilde{\chi}_v$. It was seen that structural chirality is maintained, even though the substrate is rocked in addition to rotation. At moderate values of $\delta_v$ (~ 50 % tilt with respect to $\tilde{\chi}_v$), spatial periods of the helical morphology are clearly seen, which is not

normally seen in SBD chiral films with $\delta_v = 0°$. At extreme values of $\delta_v$ (~ 80 % of $\tilde{\chi}_v$), the morphology suggests that nanocolumns resemble nano-ribbons.

It is my hope that the transmittances of tilt-modulated chiral STFs can be optimized in order to replace quarter-wave stacks with future work. Furthermore, I hope that these films can be employed to be used in passive optical elements such as beam-splitters or dichroic filters.

## 5.2 Future Work

Based on the results of the work reported in this thesis, future work can take at least three different paths.

### 5.2.1 Alternate materials

Polo and Lakhtakia based their theoretical predictions of tilt-modulated chiral STFs on empirical equations that related the relative permittivity scalars $\varepsilon_{a,b,c}$ and $\chi$ to $\chi_v$ for columnar thin films of titanium dioxide [6, 46]. Therefore, it would be of interest to fabricate tilt-modulated chiral STFs with titanium dioxide through EBPVD with the values Polo and Lakhtakia chose for $\tilde{\chi}_v$, $\delta_v$, and $\Omega$, and to compare experimental transmittances with their calculated transmittances. Even so, differences can be expected, because the relationships of $\varepsilon_{a,b,c}$ and $\chi$ to $\chi_v$ for columnar thin films are not likely to hold for tilt-modulated chiral STFs.

### 5.2.3 Changing the value of $N_{mod}$

Polo and Lakhtakia had [6] also set the number $N_{mod}$ of rocking oscillations over a structural half-period equal to 1. The value of $N_{mod}$ could be either increased or decreased by a half or whole integer. It is possible that the discrimination between circularly and linearly polarized light is futher diminished as $N_{mod}$ is increased by two or three integers, or reduced by ½.

### 5.2.3 Incident light at oblique angles

Only normally incident light was considered for calculated transmittances of tilt-modulated chiral STFs [6] and the experimental work presented in this thesis. It would be interesting to see if the suppression of the circular Bragg phenomenon is increased or decreased when the light is incident on tilt-modulated chiral STFs at oblique angles.

# REFERENCES

[1] P. G. de Gennes and J. Prost, *The Physics of Liquid Crystals,* 2nd ed., Clarendon Press, Oxford, UK (2003), pp. 271-280.

[2] A. Lakhtakia, and I. Hodgkinson, Spectral response of a dielectric thin film helicoidal bianistropic medium bilayer, *Optics Communications* **167** (1999), 191-202.

[3] V. C. Venugopal and A. Lakhtakia, On selective absorption in an axially excited slab of a dielectric thin-film bianisotropic medium, *Optics Comunications* **145** (1998), 171-187.

[4] A. Lakhtakia, Bragg-regime absorption in axially excited slabs of dielectric thin-film helicoidal bianisotropic media, *Microwave and Optics Technology Letters* **22** (1999), 243-247.

[5] Q. h. Wu, I. J. Hodgkinson, and A. Lakhtakia, Circular polarization filters made of chiral sculptured thin films: experimental and simulation results, *Optical Engineering* **39** (2000), 1863-1868.

[6] J. A. Polo Jr. and A. Lakhtakia, Tilt-modulated chiral sculptured thin films: an alternative to quarter-wave stacks, *Optics Communications* **232** (2004), 13-21.

[7] D. L. Smith, *Thin Film Deposition: Principles & Practice*, McGraw-Hill, New York, NY, USA 1995, pp. 1-7.

[8] M. Pelliccione and T-M Lu, *Evolution of Thin Film Morphology Modeling and Simulations*, Springer, New York, NY, USA, 2008, pp. 1-10.

[9] A. Rockett, *The Materials Science of Semiconductors*, Springer, USA, 1998, pp. 505-572.

[10] D. Mattox, *Handbook of Physical Vapor Deposition*, Noyes Publications, Westwood, New Jersey, USA, 2010, pp. 237-286.

[11] G. Hakansson, L. Hultman, J. Sundgren, J. Green, and W. Munz, Microstructures of TiN films grown by various physical vapor deposition techniques, *Surface and Coatings Technology* **48** (1991), 51-67.

[12] C. A. Bishop, *Vacuum Deposition onto Webs, Films, and Foils*, William Andrew Publishing, Boston, MA, USA, 2007, pp. 251-261.

[13] K. S. S. Harsha, *Principles of Physical Vapor Deposition of Thin Films*, Elsevier, Oxford, UK, 2006, pp. 431-435.

[14] M. J. Hampden-Smith and T. T. Kodas, Chemical vapor deposition of metals: Part 1. An overview of the CVD process, *Chemical Vapor Deposition* **1** (1995), 1-23.

[15] J. Plummer, M. D. Deal, and P. B. Griffin, *Silicon VLSI Technology: Fundamentals, Practice, and Modeling*, Prentice-Hall Publishing, Upper Saddle River, NJ, USA, 2000, pp. 511-513.

[16] J. R. Arthur, Molecular beam epitaxy, *Surface Science* **500** 189-217, (2002).

[17] Y. Horikoshi, M. Kawashima, and H. Yamaguchi, Low-temperature growth of GaAs and AlAs-GaAs Quantum-well layers by modified molecular beam epitaxy, *Japanese Journal of Applied Physics* **25** (1986), L868-870.

[18] L. Goldstein, F. Glas, J. Y. Marzin, M. N. Charasse, and G. LeRoux, Growth by molecular beam epitaxy and characterization of InAs/GaAs strained-layer

superlattices, *Applied Physics Letters* **47** (1985), 1099-1101.

[19] M. Leskela and M. Ritala, Atomic layer deposition (ALD): from precursors to thin film structures, *Thin Solid Films* **409** (2002), 138-146.

[20] D. P. Pulsifer and A. Lakhtakia, Background and survey of bioreplication techniques, *Bioinspiration and Biomimetics* **6** (2011), 031001.

[21] G. Decher, J. D. Hong, and J. Schmitt, Buildup of ultrathin multilayer films by a self-assembly process: III. Consecutively alternating adsorption of anionic and cationic polyelectrolytes on charged surfaces, *Thin Solid Films* **210** (1992), 831-835.

[22] A. Kumar and J. Kumar, Comentary: Layer-by-layer deposition of nanoscale structures, *Journal of Nanophotonics* **3** (2009), 030306.

[23] C. J. Lawrence, The mechanics of spin coating polymer films, *Physics of Fluids* **31** (1988), 2876-2795.

[24] M. Quirk and J. Serda, *Semiconductor Manufacturing Technology*, Prentice-Hall, Upper Saddle River, NJ, USA, (2001) pp. 256-268.

[25] S. Pursel, M. Horn, M. Demirel, and A. Lakhtakia, Growth of sculptured polymer submicronwire assemblies by vapor deposition, *Polymer* **519** (2011), 3653-3657.

[26] K. Robbie and M.J. Brett, Sculptured thin films and glancing angle deposition: Growth mechanics and applications, *Journal of Vacuum Science and Technology A* **3** (1997), 1460-1465.

[27] J. C. Sit, D. Vick, K. Robbie, and M. J. Robbie, Thin film microstructure control using glancing angle deposition by sputtering, *Journal of Materials Research* **14**

(1999), 1197-1199.

[28] D. Vick, Y.Y. Tsui, M. J. Brett, and R. Fedosejevs, Production of porous carbon thin films by pulsed laser deposition, *Thin Solid Films* **350** (1999), 49-52.

[29] L. Wei, P, P. Parhi, E. Vogler, T. Ritty, and A. Lakhtakia, Thickness-conrolled hydrophobicity of fibrous Parylene-C films, *Materials Letters* **64** (2010), 1063-1065.

[30] A. Lakhtakia, R. Messier, *Sculptured Thin Films: Nanoengineered Morphology and Optics*, SPIE Press, Bellingham, Washington, USA, 2005.

[31] R. Messier, T. Gehrke, C. Frankel, V.C. Venugopal, W. Otano, and A. Lakhtakia, Engineered sculptured nematic thin films, *Journal of Vacuum Science and Technology A* **15** (1997), 2148-2152.

[32] A. Lakhtakia and R. Messier, The past, the present, and the future of sculptured thin films, *Introduction to Complex Mediums for Optics and Electromagnetics* (W.S. Weiglhofer and A. Lakhtakia, eds), SPIE, Bellingham, WA, USA, 2003.

[33] R. Messier, V.C. Venugopal, and P. Sunal, Origin of sculptured thin filims, *Journal of Vacuum Science and Technology A* **18** (2000), 1538-1545.

[34] R. Messier, A. P. Giri, and R. A. Roy, Revised structure zone model for thin film physical structure, *Journal of Vacuum Science and Technology A* **2** (1984), 500-503.

[35] R. Messier, The nano-world of thin films, *Journal of Nanophotonics* **2** (2008), 021995.

[36] N. Young and J. Kowal, Optically active fluorite films, *Nature* **183** (1959), 104-105.

[37] P. D. Sunal, A. Lakhtakia, and R. Messier, Simple model for dielectric thin-film bianisotropic media, *Optics Communications* **158** (1998), 119-126.

[38] K. Robbie, M. Brett, and A. Lakhtakia, First thin film realization of a helicoidal bianisotropic medium, *Journal of Vacuum Science and Technology A* **13** (1995), 2991-2993.

[39] J. B. Geddes III and A. Lakhtakia, Numerical investigation of reflection, refraction, and diffraction of pulsed optical beams by chiral sculptured thin films, *Optics Communications* **252** (2005), 307-320.

[40] A. Lakhtakia, M. C. Demirel, M. Horn, and J. Xu, Six emerging directions in sculptured-thin-film research, *Advances in Solid State Physics* **46** (2007), 295-307.

[41] S. Erten, [2011], *Excitation of* I*ultiple surface-plasmon-polariton waves at metal/chiral-sculptured-thin-film interfaces*, M. Sc. Thesis, The Pennsylvania State University, University Park PA, USA.

[42] I. Hodgkinson and Q.h. Wu, Serial bideposition of anisotropic thin films with enhanced linear birefringence, *Applied Optics* **38** (1999), 3621-3625.

[43] S. Pursel, M. Horn, and A. Lakhtakia, Blue-shifting of circular Bragg phenomenon by annealing of chiral sculptured thin films, *Optics Express* **14** (2006), 8001-8012.

[44] T. H. Gilani, N. Dushkiina, W. L. Freeman, M. Z. Numan, D. N. Talwar, and D. P. Pulsifer, Surface plasmon resonance due to the interface of a metal and a chiral sculptured thin film, *Optics Express Letters* **49** (2010), 120503.

[45] A. Lakhtakia, Pseudo-isotropic and maximum-bandwidth points for axially excited chiral sculptured thin films, *Microwave and Optical Technology Letters* **34** (2002), 367-371.

[46] I. J. Hodgkinson, Q.h. Wu, and J. Hazel, Empirical equations for the principal refractive indices and column angle of obliquely deposited films of tantalum oxide, titanium oxide, and zirconium oxide, *Applied Optics* **37** (1998), 2653-2659.

[47] P. L. Jones, D. Moore, and D. R. Cotton, Optical films of single crystal zinc selenide, *Journal of Crystal Growth* **59** (1982), 183-188.

[48] I. J. Hodgkinson and Q. h. Wu, *Birefringent Thin Films and Polarizing Elements*, World Scientific, Singapore, (1997).

[49] W. D. Callister, Jr., D. G. Rethwisch, *Materials Science and Engineering: An introduction*, 8th ed., John Wiley & Sons Inc., USA, 2010.

[50] *http://www.vacengmat.com/downloads/VEM_Thin_Film_Evaporation_Guide.pdf* (last accessed 04/03/11)

[51] M. A. Hasse, J. Qui, J. M. DePuydt, and H. Cheng, Blue-green laser diodes, *Applied Physics Letters* **59** (1991), 1272-1274.

[52] M. Haggerot, H. Jeon, A. V. Nurmikko, W. Xie, D. C. Grillo, M. Kobayashi, and R. L. Gunshore, Indium tin oxide as transparent electrode material for ZnSe-based blue quantum well light emitters, *Applied Physics Letters* **60** (1992), 2825-2827.

[53] M. Danek, K. F. Jensen, C. B. Murray, and M. G. Bawendi, Synthesis of luminescent thin-film CdSe/ZnSe quantum dot composites using CdSe quantum dots passivated with an overlayer of ZnSe, *Chemistry of Materials* **8**, (1996), 173-180.

[54] T. Kostuik and M. J. Mumma, Remote sening by IR heterodyne spectroscopy, *Applied Optics* **22** (1983), 2644-2655.

[55] D. L. Huffaker, L. A. Graham, H. Deng, and D. G. Deppe, Sub-40 μA continuous-wave lasing in an oxidized vertical-cavity surface-emitting laser with dielectric mirrors, *IEEE Photonics Technology Letters* **8** (1996), 974-976.

[56] N. Kouklin, L. Menon, A. Z. Wong, D. W. Thompson, J. A. Woollam, P. F. Williams, and S. Bandyopadhyay, Giant photoresistivity and optically controlled switching in self-assembled nanowires, *Applied Physics Letters* **79** (2001), 4423-4423.

[57] M. Janotta, D. Rudolph, A. Kueng, C. Kranz, H-S Voraberger, W. Waldhauser, and B. Mizaikoff, Analysis of corrosion process at the surface of diamond-like carbon protected zinc selenide waveguides, *Langmuir* **20** (2004), 8634-8640.

[58] L. Fister, X-M. Li, J. McConnell, T. Novet, and D.C. Johnson, Deposition system for the synthesis of modulated, ultrathin-film composites, *Journal of Vacuum Science and Technology A* **11** (1993), 3014-3019.

[59] *http://www.glassdynamicsllc.com/Alkali%20Free%20Borosilicate%207059.htm* (last accessed 04/06/12).

[60] Introducing our heat-resistant kapton tapes, *Electrical Insulation Magazine, IEEE* **3** (1987), 5.

[61] *http://www.lambertopt.com/pro.asp?P_id=18* (last accessed 04/03/12)

[62]*http://www.lesker.com/newweb/Evaporation_Sources/thermal_boat_Notched.cfm?pg pg=1* (last accessed 04/03/12)

[63] S. Kasap, P. Capper, *Springer Handbook of Electronic and Photonic Materials*, 1st ed., Springer, NY USA, 325-342, (2006).

[64] N. J. Severs, Freeze-fracture electron microscopy, *Nature Protocols* **2** (2007), 547-576.

# APPENDIX

## PHYSICAL PROPERTIES OF ZnSe

**Table A.1:** List of relevant physical properties for ZnSe adopted from [63].

| **Material Property** | **ZnSe** |
|---|---|
| | |
| Melting point ($K$) | 1797 |
| | |
| Bandgap ($E_g$) | 2.7 |
| | |
| Lattice constant @ 300 $K$ | 0.567 |
| | |
| Density @ 300 K ($g\ cm^{-3}$) | 5.26 |
| | |
| Thermal conductivity ($W\ cm^{-1}\ K^{-1}$) | 0.19 |
| | |
| Poisson Ratio | 0.28 |
| | |
| Electron effective mass ($m^*/m_o$) | 0.21 |
| | |
| Hole effective mass ($m^*/m_o$) | 0.6 |
| | |
| Knoop hardness ($N\ cm^{-2}$) | 0.15 |
| | |
| Young's modulus ($Mpsi$) | 10.2 |